Distribution Agreement

In presenting this thesis or dissertation as a partial fulfillment of the requirements for an advanced degree from Emory University, I hereby grant to Emory University and its agents the non-exclusive license to archive, make accessible, and display my thesis or dissertation in whole or in part in all forms of media, now or hereafter known, including display on the world wide web. I understand that I may select some access restrictions as part of the online submission of this thesis or dissertation. I retain all ownership rights to the copyright of the thesis or dissertation. I also retain the right to use in future works (such as articles or books) all or part of this thesis or dissertation.

Signature:

_____ _____

Qiliang Liu 2020/04/15

Applications of Ultrafast Spectroscopy in Charge Transfer and Interfacial Reactions

By

Qiliang Liu

Master of Science

Chemistry

_____

Tianquan Lian

Advisor

_____

Michael C. Heaven

Committee Member

_____

Khalid Salaita

Committee Member

Accepted:

_____

Lisa A. Tedesco, Ph.D. Dean of the James T. Laney School of Graduate Studies

_____

Date

Applications of Ultrafast Spectroscopy in Charge Transfer and Interfacial Reactions

By

Qiliang Liu

B. S., University of Science and Technology of China, 2016

Advisor: Tianquan Lian, Ph.D.

An abstract of

A thesis submitted to the Faculty of the

James T. Laney School of Graduate Studies of Emory University

in partial fulfillment of the requirements for the degree of Master of Science

in Chemistry

2020

Abstract

Applications of Ultrafast Spectroscopy in Charge Transfer and Interfacial Reactions

By Qiliang Liu

Ultrafast lasers have been widely applied in various fields. As a physical method, the ultrafast laser can be utilized to study many chemical processes, such as the kinetics of chemical reactions, chemical reactions at electrode-solution interfaces, and other reactions that happen on an ultrafast time scale. In the last 4 years of my scientific research, I worked on several projects in the group using multiple ultrafast techniques. To study how the photoluminescence of a quantum nanorod is quenched on the single-molecule level, time resolved photoluminescence (TRPL) combined with atomic force microscopy (AFM) was applied to collect emitted photons from nanorods with and without contact to an AFM tip. To investigate chemical reactions in an optical cavity, transient absorption spectroscopy was performed to probe the exciton kinetics of fluorescent dye molecules trapped in a Fabry-Perot cavity. Lastly, to study the behavior of heterogeneous electrocatalyst molecules at an electrode-electrolyte interface, vibrational sum frequency generation (SFG) spectroscopy was performed to probe a monolayer of the catalytic molecules adsorbed on the electrode under a certain potential window. These projects reflect the broad applicability of ultrafast laser spectroscopic techniques on modern physical chemistry research.

Applications of Ultrafast Spectroscopy in Charge Transfer and Interfacial Reactions

By

Qiliang Liu

B. S., University of Science and Technology of China, 2016

Advisor: Tianquan Lian, Ph.D.

A thesis submitted to the Faculty of the

James T. Laney School of Graduate Studies of Emory University

in partial fulfillment of the requirements for the degree of Master of Science

in Chemistry

2020

Contents

List of Figure and Table

Figure

Table

Applications of Ultrafast Spectroscopy in Charge Transfer and Interfacial Reactions

1. Introduction

To generate the highest time resolution and capture the fastest actions, the ultrafast laser pulse, which is the shortest event, was created. The ultrafast laser has become a powerful tool in a wide range of scientific research fields to study ultrafast processes. In the physical chemistry, ultrafast lasers with femtosecond time scales can probe ultrafast chemistry. Meanwhile, its high power density and intense peak pulse energy can easily generate nonlinear optical effects, providing various probe techniques, such as time-resolved photoluminescence (TRPL), transient absorption spectroscopy (TAS), sum frequency generation (SFG) spectroscopy, or second harmonic generation (SHG). The high temporal sensitivity makes ultrafast laser spectroscopy a general characterization method as the core measurement or complementary to other experiments in pioneering research. The state-of-the-art ultrafast laser techniques developed by Lian research group were applied in my projects, presenting inclusive and abundant application of ultrafast laser in the field of physical chemistry.

1.1. Time Resolved Single-Molecule Fluorescence

1.1.1. Time-Correlated Single-Photon Counting

The time resolved photoluminescence measurement was developed based on time-correlated single-photon counting (TCSPC) techniques[1-4]. The general principle of TCSPC is to collect, at most, one emitted photon in one pulse period by a single-photon sensitive detector, such as a photon multiplier tube (PMT) or an avalanche photodiode (APD).

In a typical TCSPC setup, as shown in Figure 1.1, the emitted photons are first captured by the detector, which can be either a PMT or an APD. A randomly shaped electrical signal will then be generated by excitation of the secondary electrons on the dynodes in the PMT or the electron avalanche in the APD. Then, a constant-fraction-discriminator (CFD) precisely identifies the arrival timing of this signal by a level trigger, ensuring that the timing information is free of the influence of the varying shape and amplitude of the electrical signal. After acquiring the timing information of the signal in the CFD, which is an electrical component in the TCSPC module, the time-to-amplitude-converter (TAC) converts the timing information into the voltage amplitude of a standard electrical signal. With the reference of an input pulse or a synchronized TTL signal, the TAC starts to increase in amplitude until it receives the timing information of the emitted photon from the CFD. By extracting the amplitude value, the temporal delay of the emitted photon to the reference can be obtained. To plot the photoluminescence data, the final step is to transform all the information from an analog type to a digital type. The amplitude-to-digital-converter (ADC) realizes this transformation by registering the timing position into the digital channels (12-bit channel, equivalent to 4096 slots) according to the amplitude value from TAC. With the accumulation of the counts of the emitted photons in each slot, a histogram can be created, which is equivalent to the photoluminescence delay curves.

Usually, a pulse picker will be integrated to change the pulse period and detection time window. A typical time delay detection window can range from 25 ns to 5 μs. The time resolution of TCSPC is affected by both pulse duration and electrical response. The instrument response function (IRF) time width of a commercial TCSPC setup can range from 25 ps to 500 ps. To guarantee that no more than one emitted photon can be detected in a single pulse period, excitation is performed with low intensity and high repetition rate. Although room light and electric noise can interfere with TCSPC, it has a high sensitivity to emitted photons, fast data acquisition rate, and is relatively low cost among TRPL methods.

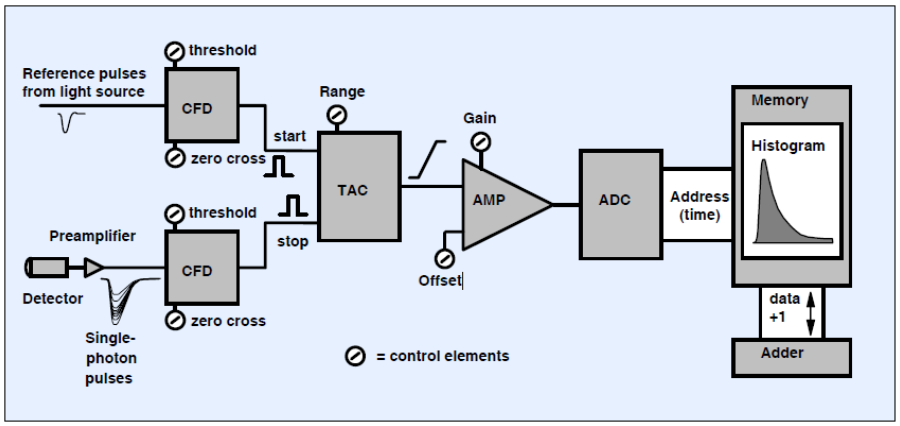

Figure 1.1. Diagram of a typical TCSPC module, including the CFD, TAC and ADC functions. Reprint from ref.[1, 3]

1.1.2. Atomic Force Microscope

Above all, TCSPC can acquire the time resolved photoluminescence of the ensemble sample. To make the detection resolution breakthrough to the single-molecule level, an atomic force microscope (AFM) is integrated with the TCSPC. TCSPC detection collects fluorescence information while the AFM offers the spatial resolution. Different from the

other optical or electron microscopes, the AFM does not scan the image by focusing the beam onto the sample surface, but instead forms a three-dimension topography of the sample surface by detecting the distance between the AFM tip and the sample through monitoring the applied force on the tip cantilever. A common schematic of the AFM is shown in Figure 1.2, where a laser beam is emitted from a laser diode and focused on the cantilever of the AFM tip. The reflected beam is collected by a position sensitive detector, and then converted to a voltage value, which contains information on deflection of the cantilever. This voltage value is further sent into a feedback loop to maintain the setpoint position of the AFM tip. A x-y piezo scanner drives the AFM tip to map the image.

There are three common operation modes: contact mode, non-contact mode, and tapping mode. In the contact mode (static mode or DC mode), the piezo scanner for the z direction is driven by a DC bias and the tip always makes a hard contact with the sample surface. The static deflection of the cantilever is mapped. In the non-contact mode (dynamic mode), the cantilever is working under the resonant vibration condition, and the modulation of sample on the cantilever is extracted from the vibration amplitude, frequency and phase. The tapping mode (AC mode) can be considered a mixture of the contact and the non-contact modes. The z direction piezo scanner is driven by an AC bias, forcing the oscillating tip to only touch the sample surface at the maximum deflection. For such a short contact time, the tip avoids sample destruction and but still records the sample topography. As the probe of AFM is determined by the shape of tip, the lateral resolution can be on the sub-nanometer scale with the sharpest tip. The usual commercial tip can reach a lateral resolution of 10~50 nm, which is much more resolved than an optical microscope.

Combining TCSPC with the AFM, the single-molecule level photoluminescence measurement can be performed.

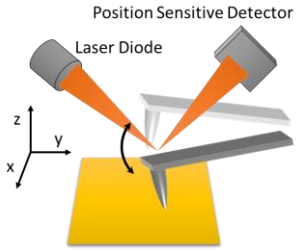

Figure 1.2. A simplified AFM schematic of tapping mode.

1.2. Transient Absorption Spectroscopy

Transient absorption spectroscopy is an ultrafast nonlinear technique in the typical pump-probe geometry. For carrier dynamics in a chemical reaction, which occur on the picosecond (10^{-12} s) or even femtosecond (10^{-15} s) time scale, a common camera is not sufficient to capture the ultrafast event. In order to probe these ultrafast events, something that can respond quickly enough would be needed which would mean using an ultrafast laser pulse to probe the modulation on another ultrafast laser pulse.

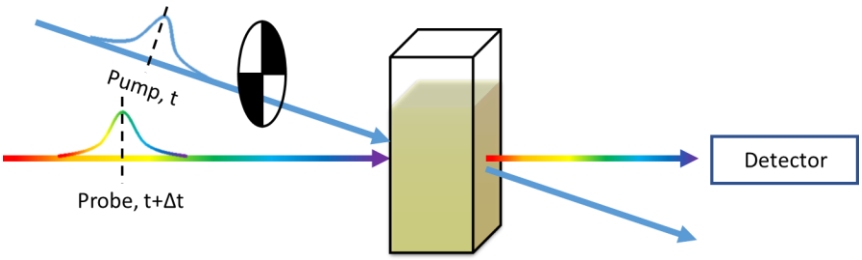

Figure 1.3. Pump-probe transient absorption spectroscopy diagram.

As an advanced absorption spectroscopy technique, transient absorption monitors the absorption spectrum change between the ground and excited states. At time zero, the

sample is excited by the pump, when the probe beam temporally overlaps with the pump (Figure 1.3). The time delay between the two beams can be controlled by a motorized stage, ranging from 0 – 2 ns, or controlled digitally by an analog synchronized signal, with the tunability up to milliseconds. A mechanical chopper is set in optical path of the pump beam and blocks every one out of two pump pulses. The ground state absorption is obtained when the pump is blocked, while the excited state is acquired with the pump unblocked. By measuring the time-delayed difference between these two absorptions, the evolution among states, such as ground states, excited states and charge transfer states, can be visualized. To increase the signal-to-noise ratio, a pulse-by-pulse reference is applied to suppress the fluctuation of the pulse, and long-time integration and averaged scans are also performed.

1.3. Vibrational Sum Frequency Generation Spectroscopy

Sum frequency generation spectroscopy (SFG) is a nonlinear spectroscopy with high surface sensitivity and selectivity. The technique was first developed by Yuen-Ron Shen and his group in 1987[5] where they observed the vibrational C-H stretching mode at both air/solid and air/liquid interface. Afterwards, electronic SFG and time resolved SFG was developed by Philippe Guyot-Sionnest to study electronic structure and dynamics of vibrational modes at different surfaces. Beyond second order harmonic generation (SHG), SFG can offer much more information about surface composition, molecule orientation and sample structure at gas-solid, liquid-solid, solid-solid, liquid-liquid and gas liquid interfaces. In a typical vibrational SFG geometry (Figure 1.4), a near IR beam (usually referred to as visible or VIS) ω_1 and an infrared beam (IR) ω_2 overlap at the sample

surface with the same timing and position. With the phase matching condition, the sum frequency beam ω_3 comes out with a certain wavelength and a certain angle.

To briefly describe the SFG selection rules, the SFG dipole can be expressed as the product of the Raman and IR dipoles, where the IR beam interacts with the sample first and excites the sample to a coherent state, and the VIS beam up converts it. Therefore, the SFG active species must be both Raman and IR active. For the IR selection rule, the coupling between the excitation beam and the vibrational mode is determined by the frequency and the direction. Therefore, modes with different orientations produce distinct amplitudes in the SFG spectrum. The orientation of a molecule at the surface can be obtained through analyzing the amplitude ratios between different modes.

The surface specification originates from the physical principles of the second order nonlinear effect. As the second order susceptibility $\chi^{(2)}$ is a third rank tensor with three subscripts representing the three axes x, y, and z in Cartesian coordinates, it has 27 independent elements if there is no symmetry limitation. Here, x and y denote the axis parallel to the surface, and z denotes the axis perpendicular to the surface. For a centrosymmetric environment like the isotropic or ambient bulk phase, due to the space inversion symmetry of the third rank tensor ($\chi^{(2)}_{i,j,k} = \chi^{(2)}_{-i,-j,-k}$) and the centrosymmetric property ($\chi^{(2)}_{i,j,k} = -\chi^{(2)}_{-i,-j,-k}$), all the elements are zero. However, for the surface, which can be thought of as having a C_∞ symmetry, four components can become non-zero independently, which are $\chi^{(2)}_{zxx}(=\chi^{(2)}_{zyy})$, $\chi^{(2)}_{xzx}(=\chi^{(2)}_{yzy})$, $\chi^{(2)}_{xxz}(=\chi^{(2)}_{yyz})$, and $\chi^{(2)}_{zzz}$. With respect to the incident surface, the *p* polarized beam contains both perpendicular (z) and parallel components (x, y), while the *s* polarized beam contains only the parallel component

(x, y). Therefore, the SFG polarization only has 4 different combinations possible for normal cases: *pss, sps, ssp, ppp* (SFG, VIS, IR).

In my project, vibrational SFG spectroscopy was applied and *ppp* polarized SFG was mainly collected under tunable applied bias. The *ppp* polarization combination is most sensitive to the modes perpendicular to the surface. Combined with orientation mapping by DFT calculations, the orientation of molecules under different bias can be extracted. Also, the vibrational Stark shift of the adsorbates can be probed by SFG, which is important for studying the interfacial electric field and how this electric field interacts with chemical reactions.

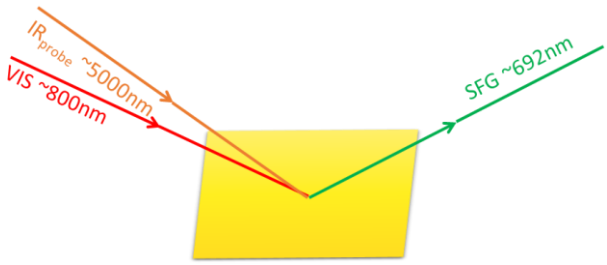

Figure 1.4. A typical near IR – visible reflective SFG geometry.

2. Single Nanorod Fluorescence Quenching by an AFM Probe

2.1. Introduction

Super resolution techniques have been useful tools to help observe dynamics and behaviors of a single particle. Among these techniques, Apertureless Scanning Near-field Optical Microscopy (ASNOM) combines the high spatial resolution from an AFM and the high time resolution from a time-resolved fluorescence microscope. By using a Pt-coated AFM probe as an electron acceptor, the fluorescence quenching was recorded when contacting a Pt coated probe with a type I CdSe/CdS nanorod. The position of contact was precisely controlled by the piezo stage and finally generated a fluorescence quenching trajectory with respect to different positions on the nanorod. The integrated PL intensity and lifetime trajectory showed that the fluorescence quenching mainly happened near the CdSe seed region.

2.1.1. Background

Colloidal semiconductor nanoscale heterostructure materials piqued people's interest for their widespread application in biological sensing[6], photocatalysis[7-11], optoelectronic device[12] and light-emitting diode[13] fields. Particularly, one-dimensional colloidal semiconductor heterostructured nanorods have proven to be very promising candidates due to their tunable light absorptions[12, 14-16] and quantum confinement effect in radial

directions and long distance (bulk-level) for long-lived charge separation[7, 10, 17-20] in longitudinal direction. For instance, CdSe/CdS dot-in-rod nanorods has been reported to efficiently produce H_2 after the growth of a platinum tip[11]. Following this discovery, a series of systematic charge transfer mechanisms have been investigated using ultrafast spectroscopy in ensemble solutions [7-10, 18, 21]. Beyond these, more valuable dynamic mechanisms of charge transfer in CdSe/CdS dot-in-rod nanoheterostructures are expected to be further developed for more advanced applications in frontier science and technology. However, ensemble-averaged spectroscopic studies are always impacted by complex components in liquid or solid systems and the inhomogeneity of sample itself[22-24]. In recent years, some super resolution optical techniques were developed to make a direct, precise and real-time observation on an individual microscale sample, such as confocal fluorescence microscopy, total internal reflection fluorescence microscopy (TIRF), stimulated emission depletion microscopy (STED), coherent anti-stokes Raman microscopy and spectroscopy (CARS), and stochastic optical reconstruction microscopy (STORM)[25-30]. These techniques provide important information that would otherwise be hidden in ensemble measurement. However, they are still faced with challenges to show their correlation with the synchronously topographic image. In an effort to improve the single-molecule measurement, the combination of topographic and optical measurements becomes essential for better understanding more mechanisms in nanostructures[22-24].

One kind of novel high-resolution technique to overcome the optical diffraction limit is Apertureless Near-field Scanning Optical Microscopy (ASNOM)[31]. In ASNOM, an AFM probe offers photo-physics information, such as fluorescence[22, 32-33], Raman scattering[34-38], and back scattering[39-42] with spatial resolution. In addition, with a functionalized AFM tip,

including QD[23-24] and carbon nanotube modified tips[43], single nanoparticle charge transfer and energy transfer mechanisms between modifiers on tips and molecules on substrates can be explored. Being mounted on an inverted fluorescence microscope, the AFM-fluorescence microscope setup can record the correlated topographic and photoluminescent image simultaneously.

Significant efforts have been devoted to the study of charged carrier kinetics of ensemble CdSe/CdS quantum nanorods by various ultrafast spectroscopies[8, 17-18, 20-21, 44], which provides knowledge of the charge transfer and charge separation process with time evolution. Beyond that, the carrier kinetics of a single quantum dot particle can be further revealed by a time resolved fluorescence microscope with manipulation by an AFM probe[22-24]. Due to the advantages of single-molecule detection, the interference from the size distribution, defects, and other inhomogeneous broadening effects can all be eliminated. The most straightforward fluorescence decay kinetics of a single CdSe/CdS nanorod, can be probed by our single molecule measurement, which offers new sights into quantum nanorod fluorescence quenching.

2.1.2. Purpose and Expectation

In this project, the CdSe/CdS dot-in-rod nanorod is used as a model to imitate the charge transport in one-dimensional nanoscale device. After selectively exciting the exciton in the CdSe core, the electron will experience the 1D random walk in the longitudinal direction of the CdS rod before radiative decay with the hole remaining in the CdSe core. With the Pt tip as an electron acceptor, the fluorescence of CdSe/CdS will be quenched. By monitoring how the fluorescence is quenched depending on Pt tip position to the CdS core,

the electron diffusion in CdS rod is mapped out. The scheme is shown in Figure 2.1. Compared with direct deposition of Pt on the tip of CdSe/CdS[8, 17], using an AFM tip as the electron acceptor can circumvent length distribution inhomogeneities in the solution ensemble and also provide better distance control. In this project, the process of electron transfer from a potential well (CdSe seed in CdSe/CdS nanorod) to an electron acceptor (Pt coated tip) was imitated by an AFM probe contact. The results demonstrated that the fluorescence was mainly quenched near the CdSe seed region. Simulations were also applied to understand the position-dependence of the fluorescence quenching.

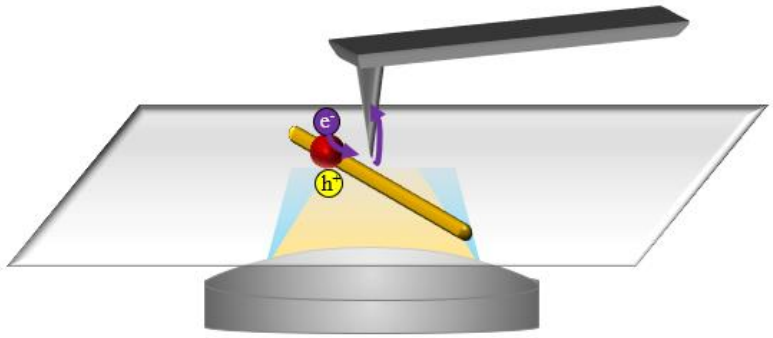

Figure 2.1. Schematic of the single-molecule correlated AFM and fluorescence setup.

2.2. Experiment Methods

2.2.1. Synthesis of CdSe/CdS dot-in-rod

The dot-in-rod nanostructure CdSe/CdS nanorods were synthesized by a previously reported method[14]. Briefly, the wurtzite CdSe seeds were first synthesized and then CdS precursor were added and the seeds were allowed to grow into a rod nanostructure. CdO (0.060g), ODPA (0.280g) and TOPO (3g) were mixed in a 3-necked round bottomed flask. After being kept at 150°C in vacuum for an hour, the temperature was increased to 320°C

to dissolve CdO until a clear solution was formed under nitrogen. A Se precursor (0.060g Se in 0.5ml TOP) was swiftly injected into the flask after the temperature was heated up to 370°C. The size of the CdSe seeds were determined by the reaction time after Se injection. Typically, 3.6 nm CdSe seeds were achieved with a reaction time of approximately 30 s. CdSe seeds were washed by precipitation and redispersed in toluene and ethanol and finally dispersed into hexane.

The nanorod was synthesized via the seeded growth approach[14, 18]. For 140 nm CdSe/CdS dot-in-rods, CdO (0.093g), HPA (0.080g), ODPA (0.290g) and TOPO (3g) were mixed in a 3-necked flask. The temperature was heated up to 350°C under nitrogen protection after 1h of degassing under vacuum. Then 1 mL TOP was added to flask. The S precursor solution was prepared by dissolving 100 nmol CdSe seeds and S (0.060g) in 1 mL TOP. The resulting solution was quickly injected into the flask and allowed to react for 8 min. The nanocrystal was purified by precipitation and redispersion in toluene and ethanol, and finally dispersed into toluene.

The high quality CdSe/CdS dot-in-rods in this project were provided by Dr. Pyun's group from Arizona University. Sample characterization including UV-vis absorption and transmission electron microscope (TEM), which are shown in Figure 2.4.

2.2.2. Sample Preparation

To measure the nanorod on the single-molecule level, we serially diluted the nanorod solution to a suitable concentration (~1 pM) by adding 100 μL of 1 nM nanorod solution into 1 mL toluene solution 3 times. The diluted CdSe/CdS nanorod solution (50 μL) was spin-coated (1500 rpm, 3 s) onto a glass coverslip precleaned with water, acetone, and

ethanol. The toluene would typically volatilize resulting in nanorods that were homogenously dispersed on the dried glass coverslip.

2.2.3. Single-Molecule Quenching Experiment Setup

Typically, we measured an individual sample by scanning correlated AFM and fluorescence images. A schematic of the synchronous surface scanning probe and fluorescence microscope set-up was demonstrated in the Figure 2.2. An AFM terminal (Asylum MFP-3D) was mounted on an epi-fluorescence microscope (Olympus IX70) equipped with a 100×1.4 NA oil immersion objective (Olympus). A Ti:Sapphire (Tsunami oscillator pumped by a 10 W Millennia Pro, Spectra-Physics) laser system generated an ultrafast laser pulse (~100 fs) with a 80 MHz repetition rate where the wavelength was centered at 980 nm. To ensure the sample was only excited once in one PL decay period, the laser beam was sent through an electro-optical modulator (Conoptics, USA) to reduce the repetition rate to 4 MHz, which changed pulse period from 12.5 ns to 250 ns. Then, the laser output was doubled to 490 nm by a Type II BBO crystal. As shown in the Figure 2.2, the glass coverslip spin coated with CdSe/CdS nanorods was then fixed onto the x-y plane scanning stage. The excitation beam was tuned from 80 nW to 200 nW and focused down onto the sample coverslip. When the integrated topographic and photoluminescent image was performed, the x-y plane piezo stage was moving while the AFM probe and the excitation beam focus were relatively settled at a stationary position. The height, amplitude, and phase trace were collected simultaneously by the AFM head, and a fluorescence trace was detected by the avalanche photodiode (APD, PerkinElmer SPCM-AQR-14). The PL signal outputted by the APD was further analyzed by a time-correlated single photon counting (TCSPC) module and corresponding software (Becker & Hickl, SPC 600). The

IRF full width at half maximum was approximately 600 ps. A single nanorod fluorescence decay was treated as a simple single-exponential decay. This measurement can be performed under both room temperature in air or a sealed system with nitrogen protection.

To reach a sub-diffraction limit resolution and reveal the length dependence fluorescence quenching of a ~140 nm nanorod, an AFM tip was used due to it being an excellent quenching medium[22], as well as offering high resolution topographic images. In order to quench the CdSe/CdS dot-in-rod fluorescence emission by the AFM probe, a silicon based, platinum coated AFM tip (MIKROMASCH HQ:NSC35/Pt) was chosen to be the quenching antenna, which works by trapping excited electrons into the Pt layers[8, 17, 45]. The AFM images were scanned in the intermittent mode (tapping mode or AC mode). CdSe/CdS nanorod PL emission was quenched through physical contact with the Pt coated tip through contact mode.

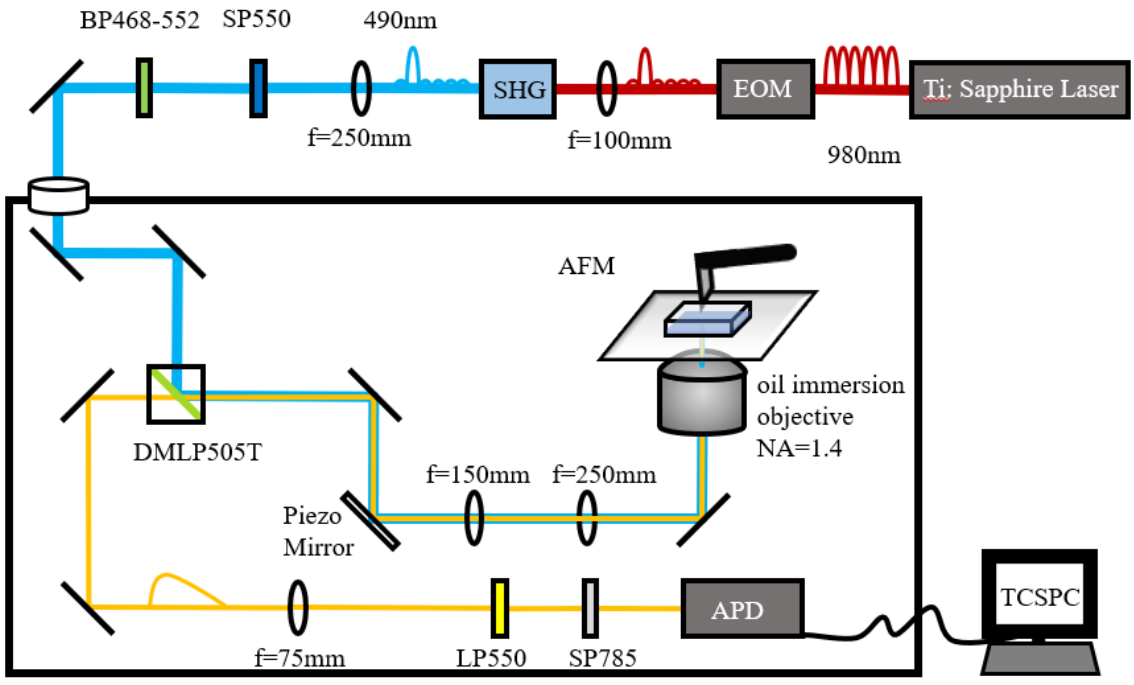

Figure 2.2. Schematic of the single-molecule measurement setup

To simultaneously make the comparison between free nanorod PL decay and quenched nanorod PL decay, the AFM probe and excitation beam focus were aligned onto the same position. Since the AFM probe and excitation beam focus were stationary while the piezo scanning stage was in motion and the AFM probe and the excitation beam focus were collecting data at a random location for the initial scan trial, if the AFM tip was not overlapped with the excitation beam focus location, the corresponding PL decay data could not be recorded while AFM tip was in contact with the CdSe/CdS nanorod. The strategy to align the AFM tip together with excitation beam focus was based on matching the similar height trace and fluorescence patterns in AFM image and PL image respectively, following previous literature[23-24]. Figure 2.3 a-c describes the alignment procedures. Firstly, the excitation beam was tuned to focus roughly near the tip location, based on the real time optical microscope camera integrated with the epi-fluorescence microscope. The position of the tip on the AFM probe cantilever was estimated through the probe product information. Typically, a $30 \times 30\ \mu m^2$ area on the sample coverslip was scanned by AFM and fluorescence microscope at the same time. By marking all the fluorescence patterns one by one, a similar height trace pattern in AFM image could also be extracted. The height trace in the AFM image might not indicate nanorods but might instead indicate impurities; the fluorescence trace must originate from fluorescent nanorods emitting light. If the fluorescence pattern was able to match with the height trace pattern, PL of the CdSe/CdS nanorod, the morphology, and the surroundings could be all detected to avoid introducing impurities into the single-molecule measurement. Meanwhile, the displacement of AFM image pattern and PL image pattern represented the displacement of the location of the AFM probe tip and excitation beam focus. By operating the piezo mirror, the excitation

beam focus could be moved close to the AFM probe tip empirically. After the initial scanning, the scanning area was zoomed in to a 10 × 10 μm^2 area for a more precise alignment. Finally, the scanning area was zoomed in to an individual CdSe/CdS nanorod with a typical scan area of 500 × 500 nm^2. For each image, the size was set to 256× 256 $pixels^2$ and scanned back and forth with a rate of 0.13 Hz. The APD photon integration time was set to 20 ms which matched the scan rate and guaranteed that for each pixel point, the scan time and photon collection time was roughly identical.

After the AFM tip and excitation beam focus were well aligned and the scan area was zoomed into an individual CdSe/CdS nanorod, the scan rate was set to 0.50 Hz and the excitation beam was blocked to scan this nanorod multiple times until the AFM image was reproducible. In this case, the AFM was switched to contact mode. The AFM tip was moved into position along with the nanorod. The non-quenching and quenching PL intensity and lifetime trajectory were measured by recording photons by TCSPC when AFM tip was not engaged and when it was engaged and physically made hard contact with the nanorod. For the nanorod, each data point contained 15 s PL intensity and the lifetime trajectory for preventing the nanorod degrading under continuous light illumination. When the CdSe/CdS nanorod was excited and electrons were trapped by the Pt coated tip contact, the holes were trapped in the CdSe seed, where they were consumed by oxygen in the air and easily oxidized the CdS rod in the atmosphere. To enhance the luminescence stability, an enclosure was made by wrapping saran wrap around the setup for nitrogen purging in order to oxygen (Figure 2.3 d). After collecting the PL trajectory at one position, the AFM tip was withdrawn and moved to the next adjacent position, to avoid any destructive impact

on the nanorod. Finally, the PL intensity and lifetime trajectories of each position were combined to generate the whole data set.

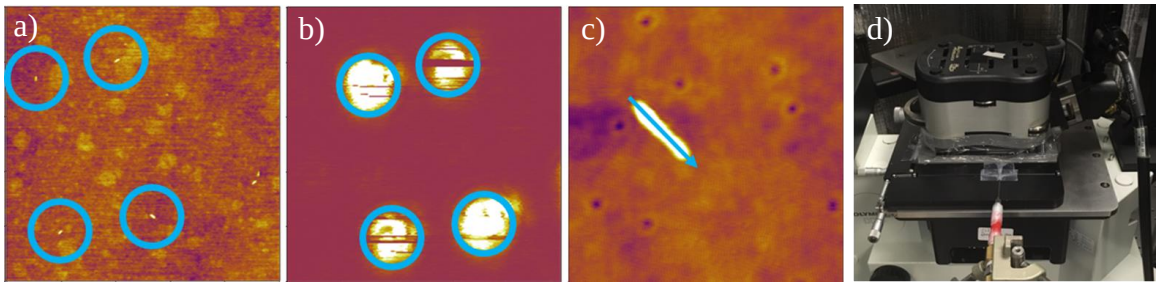

Figure 2.3. a), b) and c) Description of AFM tip and excitation beam focus alignment procedures; d) A closed scan stage wrapped by the cling film with the nitrogen purge system.

2.3. Results and Discussion

The CdSe/CdS dot-in-rods, as mentioned above, were shown to have an average length of 141.0 ± 7.1 nm and an average width of 5.3 ± 1.2 nm determined by a TEM photograph (Figure 2.4 a). Figure 2.4 b shows the absorption and PL emission spectra of these nanorods. By estimating the bandgap of the CdSe seeds with 3.6 nm diameter, using the empirical extinction coefficient extracted from the CdSe 1S absorption peak[46], these $CdSe_{3.6nm}/CdS_{141nm}$ heterostructured nanorod could be considered to have a Type I alignment nanostructure, based on published theoretical calculation results[47-48]. The Type I band alignment between the CdSe core and CdS rod results in the confinement of electron-hole pairs into the CdSe core[49], because of the energy level well from the fall of valance band and conduction band at the interface between CdSe and CdS.

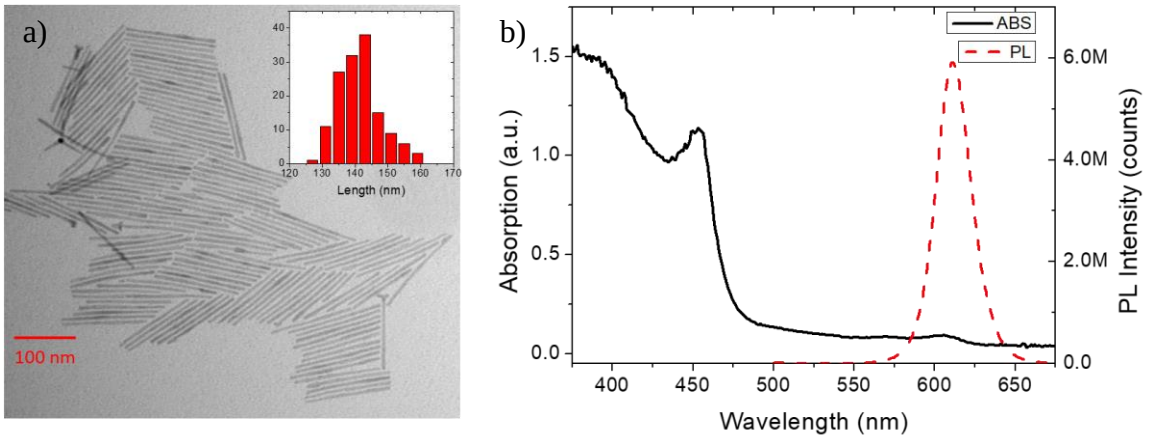

Figure 2.4. a) TEM photography of CdSe/CdS dot-in-rod nanorod; b) Absorption and emission spectrum of CdSe/CdS nanorod. Absorption under 500 nm was from the CdS rod; two weak peaks at 570 nm and 605 nm was the CdSe seed absorption.

Figure 2.5 a depicts the AFM image of a single CdSe/CdS nanorod with an image size of 500 × 500 nm^2. The AFM image contained some black holes and background substrate impurities, which could be relatively considered as surface contamination[50] from spin coating and some residual organic precursor. From the PL image during alignment procedure with a larger image size (Figure 2.5 b), it had been verified that these artifacts would not interfere with the PL measurement. In addition. Figure 2.5 c also showed that in the range of optical diffraction limitation, there was not any other emission, which supported that this was measured on the single-molecule level. The AFM height trace shows the CdSe/CdS nanorod with a length of 148 nm (FWHM) and a width of 21 nm (FWHM). The upper left part of the nanorod was extended and bent a little, which could be considered as the CdSe seed region.

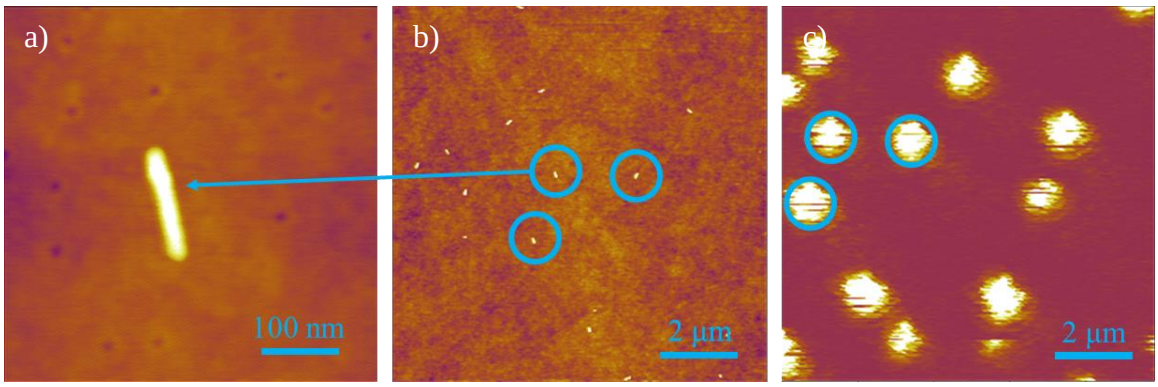

Figure 2.5. a) AFM image of a single CdSe/CdS dot-in-rod nanorod. b) Large size AFM image for alignment. c) Correlated PL image with b).

Figure 2.6 a shows integrated PL intensity and lifetime trajectory of the free state (no Pt tip contact, setpoint = 0.000V) and contact state (engage Pt tip contacted with nanorod, setpoint = 0.200V) at different positions along with the nanorod. In contact mode, the AFM probe tip-to-sample distance could be checked by the feedback of the deflection, which was identical to the displacement of the tip from the released state (setpoint =0.000V). The deflection would be well maintained when adding a setpoint over 0.050V. Therefore, setpoint of 0.200V could be considered as having good physical contact between the Pt coated tip and the CdSe/CdS nanorod.The free state PL intensity and lifetime trajectory were collected repeatedly; then the AFM tip was engaged for collecting contact state PL intensity and lifetime trajectory; afterwards, AFM tip was released and moved to the next position. The point marks in Figure 2.6 a corresponds to the markers shown in the correlated AFM image in Figure 2.6 c. Basically, the AFM tip was scanned from the upper left to the bottom right parts of the nanorod. Spacing between two steps was 11.5 nm on average. The free state PL intensity trajectory (black solid lines) was maintained in the range 200~300 counts per 50 ms in positions 1-5, while it was reduced gradually in

positions 6-10, and finally kept stable between 50~150 counts per 50 ms in positions 11-14 as shown by the black line in Figure 2.6 a. Similarly, the contact state PL intensity trajectory also shows the trend of gradual decrease and final stabilization. By comparing these two trends, the PL intensity was quenched somehow in positions 2, 3, 4, 5, 6, 7, and 8 by the Pt coated tip contact. The tip enhanced fluorescent emission was reported in some published literature[22, 32-33] with a similar apertureless near-field optical microscope, however, this phenomenon was not clearly understood and did not appear in this experiment. The PL intensity consists of many components, indicating many complicated processes, making it difficult to identify each component and extract useful information from the PL intensity trajectory in this case[51]. Also, taking the length of nanorod into consideration, 140 nm was within the same diffraction limitation because the only changing parameter when collecting data at the free state was the position. When the AFM tip was moved to a position, in fact, the piezo scan stage was moving to a new position and the relative position of AFM tip and excitation beam focus was not changed. Therefore, one possible reason for the gradual reduction of the PL intensity might be that intensity distribution of the excitation beam focus varied at different positions; On the other hand, with increasing time, the surface defects or trapping states might slowly form and cause the PL intensity decrease.

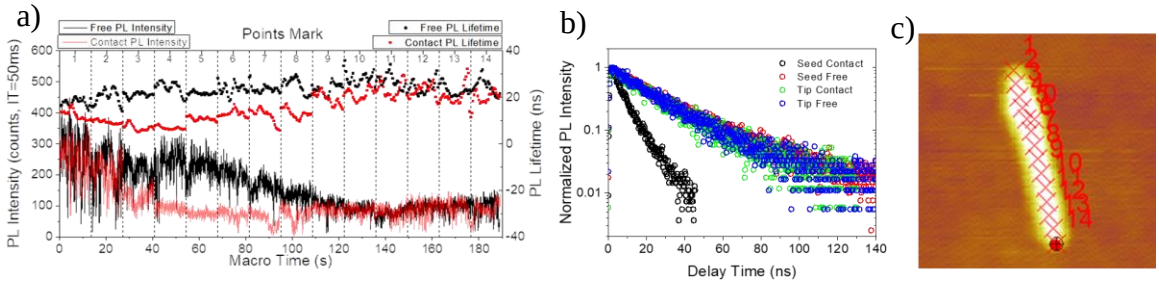

Figure 2.6. a) Integrated PL intensity and PL lifetime trajectories. Free state is marked black and the contact state was marked red. Line indicated PL intensity trajectories while dots indicated PL lifetime trajectories. b) PL decay curve at free and contact state at seed and rod tip location. c) The corresponding points markers in AFM image, associated with contact position.

While it was unclear how to analyze the PL intensity, the PL intensity decay curves and PL lifetime would be much more straightforward and useful. In Figure 2.6 a, black dots indicate the free state PL lifetime and red dots indicate the contact state PL lifetime, both of which were obtained by fitting with the IRF convoluted single-exponential (some featured decay curves are shown in Figure 2.6 b). The free state PL lifetime was within 15~30 ns. To contrast, the contact state PL lifetime showed an obvious reduction in positions 2, 3, 4, 5, 6, 7, and 8 (the lowest points was 6~7 ns), and did not show much difference at the other locations compared with the free state PL lifetime. At the contact state, the PL lifetime reduction region was overlapped with the PL intensity quenching region. Obviously, positions 2, 3, 4, 5, 6, 7, and 8 were found near the CdSe core region based on the markers in correlated AFM image (Figure 2.6 c) when doing the quenching experiment. This showed that PL intensity population was reduced when the nanorod contacted with a Pt coated tip only near the CdSe core region.

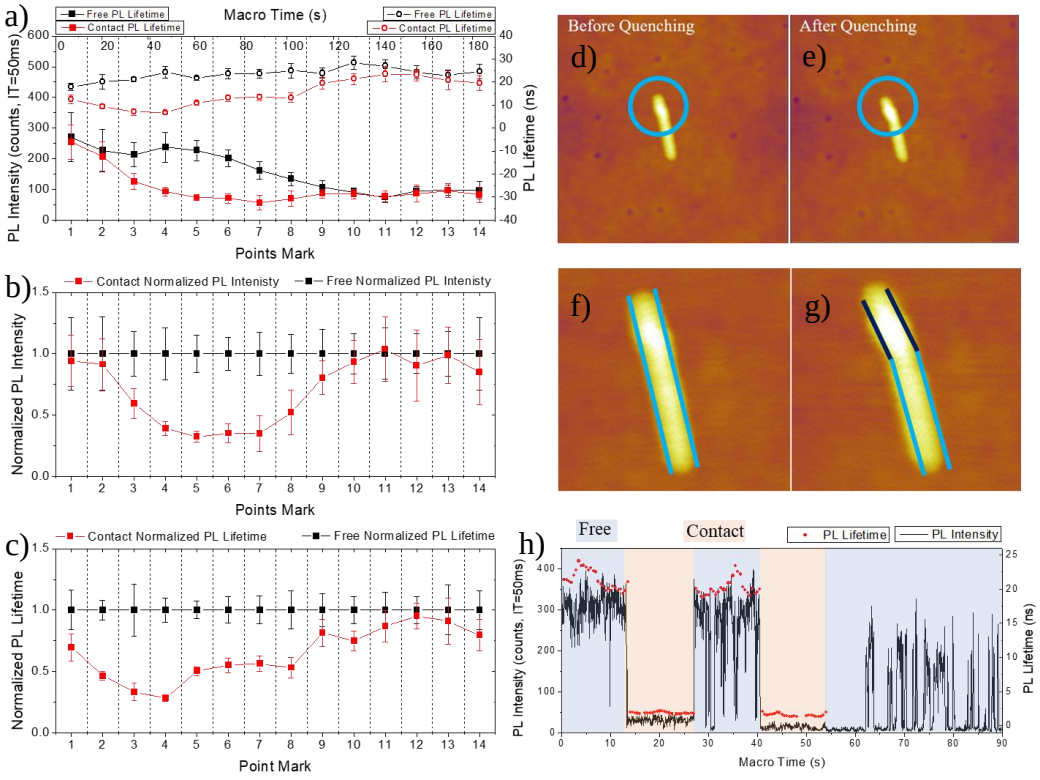

Figure 2.7. a) Integrated mean PL intensity and lifetime trajectory. b) Normalized PL intensity trajectory. c) Normalized PL lifetime trajectory. d) The CdSe/CdS nanorod AFM image after first scan with Pt contact, before second backward scan. e) The degraded nanorod AFM image. f) Diagram of the normal shape of the nanorod. g) Diagram of the degraded shape of the nanorod. h) PL intensity and lifetime trajectory when degradation happened. Blinking behaviors increased remarkably.

To understand the integrated PL intensity and lifetime trajectory better, these trajectories were further analyzed statistically. As shown in the Figure 2.7 a, the “on” state PL intensity and lifetime trajectory at each point were replaced by their mean intensity and mean lifetime for the “on” state, with error bars set as standard deviation. The “off” state was selectively neglected. The statistically integrated PL intensity and lifetime trajectory kept the same trend as the integrated trajectory. At this point, I assumed that the intrinsic

fluorescence decay of CdSe/CdS nanorod maintain unchanged with respect to different position if no electron transfer happens. The amplitude of fluorescence which scales with the excitation intensity can be regarded unchanged when moving the sample due to the relatively large beam size compared with rod length. Based on equations 2.1 and 2.2[51]:

$$I_{free} \propto \frac{k_r}{k_r+k_{nr}}\left[A_{0,free}\right] \textbf{ eq. } (2.1) \qquad I_{contact} \propto \frac{k_r}{k_r+k_{nr}+\Delta}\left[A_{0,contact}\right] \textbf{ eq. } (2.2)$$

$$\tau_{free} \propto \frac{1}{k_r+k_{nr}} \textbf{ eq. } (2.3) \qquad \tau_{contact} \propto \frac{1}{k_r+k_{nr}+\Delta} \textbf{ eq. } (2.4)$$

I represents the total PL intensity count over integration time. A_0 represents the initial exciton population in CdSe core after excitation. k_r , k_{nr} and Δ represent decay contribution from radiative decay, non-radiative decay and Pt quench. All the free state mean PL intensities were then normalized with respect to itself. All average PL intensities at different contact states were then scaled with respect to free state mean PL intensity. Similarly, the statistic PL lifetime could be normalized based on equations 2.3 and 2.4[51]. The scaled average PL Intensity and lifetime trajectory was plotted in Figure 2.7 b and c. Scaled average PL intensity trajectory shows an obvious quenching of PL intensity at positions 3, 4, 5, 6, 7, 8; Meanwhile, the scaled average PL lifetime trajectory shows a reduction of lifetime, which means a faster PL decay process, at positions 1, 2, 3, 4, 5, 6, 7, and 8. Corresponding to the point markers in the contact mode AFM image, both of these position sets were around the CdSe seed region, supporting that CdSe/CdS nanorod fluorescence was only quenched nearby the CdSe seed region. In addition to verify its repeatability, a second trial was scanned. Unfortunately, the nanorod degraded this time even under nitrogen protection (shown in Figure 2.7 d, e, f, g, h). It was necessary to purge

nitrogen to prevent the degradation. Otherwise, it would have impacts on the PL intensity and lifetime trajectories.

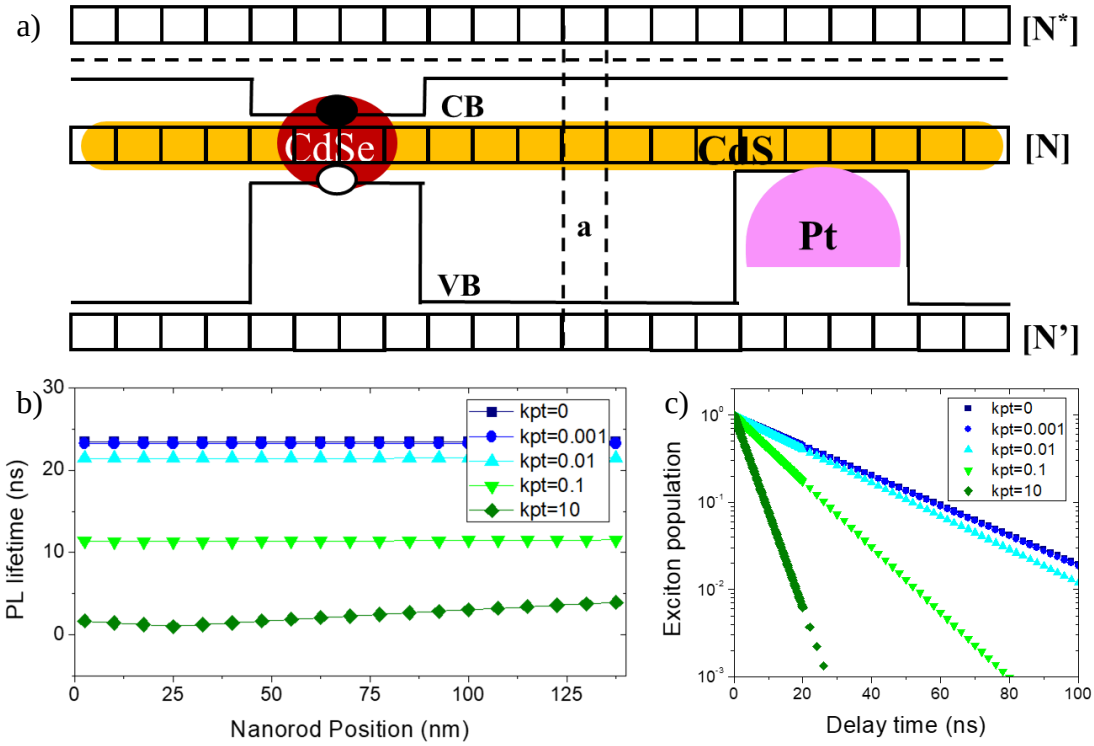

Figure 2.8. a) Simulation model. b) Simulated PL lifetime trajectory with respect to different Pt contact position with different electron trapping rate k_{pt}. Seed was set at 25 nm. k_{pt} = 0 means free state. c) single exponential decay with different k_{pt}.

To explicitly model this fluorescence quenching trend, a simulation model[52-53] was applied to show the PL intensity decay curve with respect to different electron transfer rates to Pt (Figure 2.8 a). Briefly, when absorbing light, the CdSe core was excited to generate an exciton inside. It was denoted that the initial exciton population was 1 in the CdSe seed and 0 in CdS rod. The exciton in the CdSe seed has a chance to be ionized into a free electron and a confined hole[54] – the electron is not associated with the hole and could freely diffuse in all directions along with the nanorod while the hole is still trapped in CdSe seed.

When free electrons came across with Pt coated tip, electron trapping occurred. The simulation model is given below:

$$\frac{\partial [N^*](i,t)}{\partial t} = -D\frac{\partial \frac{\partial [N^*](i,t-1)}{\partial a}}{\partial a} = -D\lim_{a\to 0}\frac{\frac{[N^*](i,t-1)-[N^*](i-1,t-1)}{a} - \frac{[N^*](i-1,t-1)-[N^*](i,t-1)}{a}}{a}$$

$$\cong -D\frac{2[N^*](i,t-1)-[N^*](i-1,t-1)-[N^*](i+1,t-1)}{a^2}, \quad \frac{D}{a^2} = k_d \qquad \textbf{eq.}\ (2.5)$$

$$\Delta[N](i,t)/\Delta t = -k_i[N](i,t-1) - k_r[N](i,t-1) - k_{nr}[N](i,t-1) + k_b[N^*](i,t-1) \qquad \textbf{eq.}\ (2.6)$$

$$\Delta[N^*](i,t)/\Delta t = k_i[N](i,-1) - k_b[N^*](i,t-1) - k_d\big(2[N^*](i,t-1) - [N^*](i-,t-1) - [N^*](i+1,t)\big) - k_{pt}[N^*](i,t) \qquad \textbf{eq.}\ (2.7)$$

$$\Delta[N'](i,t)/\Delta t = k_{pt}[N^*](i,t) \qquad \textbf{eq.}\ (2.8)$$

Among this model, N, N^*, and N' represent the exciton population, ionized electron population and trapped electron population relatively. Diffusion constant D was estimated by electron mobility μ_e in bulk CdS[55]:

$$\mathrm{D} = \frac{\mu_e kT}{e} \qquad \textbf{eq.}\ (2.9)$$

where k is Boltzmann constant and T is room temperature 300K. a, the Bohr radius of the electrons in bulk CdS as the minimum moving step for free electrons is given by[56-57]:

$$a = \frac{4\pi\varepsilon\hbar^2}{m_e^* e} \qquad \textbf{eq.}\ (2.10)$$

where m_e^* is the effective mass of the electrons in bulk CdS.

Other parameters were relatively estimated as: ionization rate k_i as 0.1 ps^{-1}, ionized electrons binding recombination rate k_b as 200 ps^{-1}, total radiative decay and non-radiative

decay rate k_r as 0.00004 ps^{-1}, diffusion rate k_d as 125 ps^{-1}, and electron bohr radius a as 2.5 nm. Different electron transfer rate to Pt. k_{pt} was tuned as 0, 0.001, 0.01, 0.1, 10 ps^{-1}. The simulated lifetime (fitted by single exponential decay model) with respect to different position were shown in Figure 2.8 b. The seed position was settled to 25 nm. As trapping rate was very slow, lifetime did not have reduction and position dependence; While trapping rate was as high as the one in Pt-tipped CdS nanorod[7] (k_{pt}= 0.1 ps^{-1}), a decrease of lifetime without position dependence showed. Even if k_{pt} was tuned to 10 ps^{-1}, a weak position dependence showed, but with a very short lifetime. Figure 2.8 c shows the simulated decay curve to verify the single exponential decay. The faster electron trapping rate caused the shorter lifetime.

Taking into account the previous results (shown in Figure 2.9 a-d) from Arshad Karumbamkandathil, a previous group member who worked on this project, his results showed a non-position dependent fluorescence quenching trend. However, I believed that his results required some further work to be complete. Firstly, his work was done in the atmosphere and he did not verify the CdSe/CdS nanorod stability after the Pt contact. The nanorod might probably have degraded and showed that quenching trend. Moreover, the CdSe/CdS nanorods absorption spectrum did not show a typical CdSe seed absorption, which indicates this sample might be sort of $CdSe_xCdS_{1-x}$ alloyed heterostructured nanorods. If so, the assumption that exciton was only generated from the CdSe seed was no longer applicable. This irregular excitation might result in a non-position dependent fluorescence quenching. In fact, Banin's group published the similar results based on similar techniques[22]. As shown in Figure 2.9 e-h, a lifetime image of a 108 nm CdSe/CdS nanorod was scanned by a Pt coated tip under AFM tapping mode. The fluorescence

quench was only observed near the CdSe seed region. A possible explanation of this result was proposed that the electron-hole pairs might have a leakage to the Pt coated tip when the AFM probe oscillating at the lowest case where it was nearly contacting with the nanorod. In my project, a hard engage was applied to make sure Pt coated tip was fully contacted with the nanorod. However, the interface of the tip and nanorod was unclear. Particularly, CdSe/CdS colloidal nanorods are always containing large amounts of ligands on the surface. How these ligands will make contributions to the fluorescence quenching is still a question that needs to be answered and would require the development of more advanced techniques.

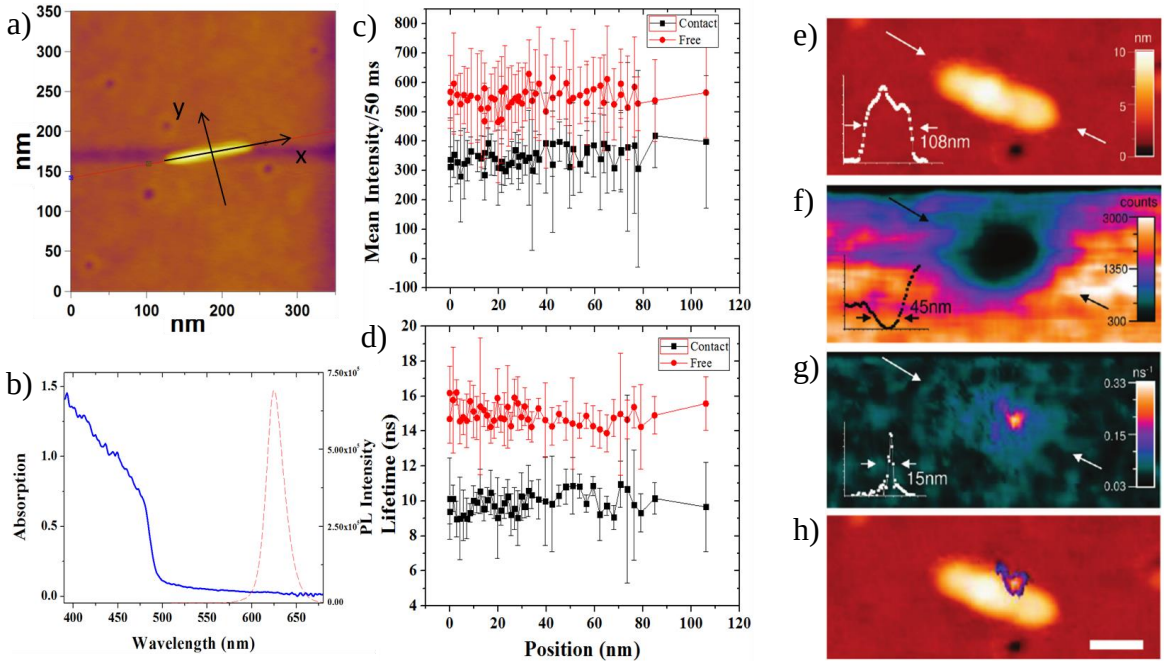

Figure 2.9. a-d) Arshad's work on this project. e-h) Banin's group published results. Reprint from ref.[22].

2.4. Conclusion

In conclusion, a single molecule technique setup was applied in this project to reveal the determining step in a one-dimensional electron transfer model. However, the results did not agree with our hypothesis. It seemed that the fluorescence quenching was not merely from the electron trapped to Pt, but also contained energy transfer contribution, especially near the CdSe seed region. Further work to reveal the interfacial structure and impact of ligands needs to be done to understand this result more clearly.

In the future, the potential of our current integrated AFM and fluorescence microscope will be developed. One of the interesting applications of this setup is to transfer it to measure single particle time-resolved electro-luminescence. In recent years, colloidal semiconductors have been developed for many electro-optical devices. Among them, light-emitting diodes (LEDs) are a very hot topic[13]. To understand the internal mechanism of electroluminescence, people measure transient electroluminescence emission spectra in microsecond scale. While time-resolved PL measurement is mainly measured by TCSPC method, which counts single photon events in every pulse period. This pulse period is identical as pulse picker's setting, which is controlled by a periodical electronic signal. Analogous to time-resolved PL measurement, if the periodical electronic signal could trigger a correlated DC current, which goes through conductive coverslip and AFM probe to generate a circuit, then the nanosecond resolution electroluminescence could be recorded theoretically. By ALD, electron transfer layers or hole transfer layers are able to grow on the AFM probe and coverslip. Hopefully, through a clearer and higher temporal resolution electroluminescence kinetics, LED device field could be pushed to a more advanced level.

3. Molecules in Optical Cavity with Light-Matter Strong Coupling

3.1. Introduction

3.1.1. Background

The molecules with an exciton transition located in an optical cavity can generate a hybrid light-matter state with the localized light, called exciton-polariton, which has half light-half excitonic properties[58-61]. The formation of this light-matter interaction requires resonantly matched molecular optical transitions and corresponded cavity modes. The strong coupling between the exciton transition and localized electric field in the cavity rises up the splitting of the energy, known as Rabi splitting. The corresponded two new polaritonic states (P+, P-) are mixed states of light and exciton, as illustrated in Figure 3.1. With the electric field $\vec{E}$ and dipole moment $\vec{d}$, n_{ph} photons in a cavity with volume V at vacuum (permittivity = ε_0) will have a Rabi splitting as described equation 3.1[58, 60, 62-69]:

$$\hbar\,\Omega_{Rabi} = 2\vec{E}\cdot\vec{d}\cdot\sqrt{n_{ph}+1} = 2\sqrt{\hbar\,\omega/\varepsilon_0 V}\,d\sqrt{n_{ph}+1} \qquad \text{eq. (3.1)}$$

As an analog to the molecular orbit diagram, the photons in the optical cavity are quantized photons, like harmonic oscillators with certain frequency and limited boundary. The newly formed polariton states are the results of coupled photons and transitions.

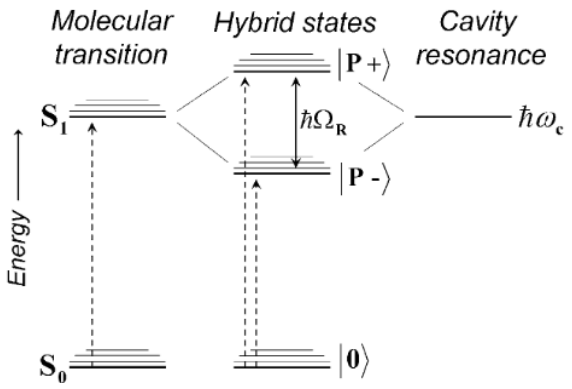

Figure 3.1. Interpretation of hybrid light-matter states. Reprint from ref.[68]

The coupling strength is determined by the density of the coupled electric dipole and the quality of the cavity. With the benefit of that, the light-matter strong coupling regime can be easily achieved through two main ideas: a planar Fabry-Perot cavity containing a large number of molecules[60, 63, 69-85] or a single emitter enclosed in a high-quality nanocavity[86-96]. In addition, to achieve strong coupling there is no need to compromise to low temperature or high vacuum condition based on light-matter interaction. As the shown in the Figure 3.2, the former cavities are photonic and the latter ones are plasmonic cavities. Both types have diverse species that can generate a resonant optical mode compliable for different requirement.

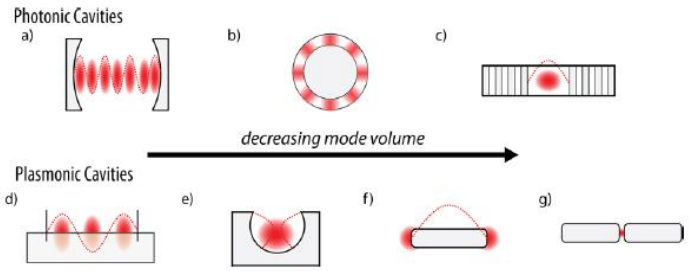

Figure 3.2. Photonic cavity forms: a) Fabry-Perot cavities, b) resonators, c) Bragg gratings or photonic crystals; Plasmonic cavity forms: d) trapped standing wave or surface plasmon, e) and f) localized surface plasmon, g) nano antenna. Reprint from ref.[59]

The physics of the exciton-polariton has been well studied, while the interest of modification of chemical reactions of the molecules in the optical cavity have become more and more attractive. Thomas Ebbesen and his students inspire many perspectives and lead the pioneering studies in this field[60, 62-69, 71, 77, 80, 82, 92, 97-115]. They studied the ground state chemical reactivity of the silane deprotection reaction of 1-phenyl-2-trimethylsilylacetylene, and retardation of the reaction rate was reported under vibrational strong coupling[65]. They also manipulated the donor and accepter energy level by strong coupling in an optical cavity, to increase the resonant energy transfer rate[64]. They also explored the possibility of the strong coupling application out of the optical purpose. By fabricating the organic semiconductor on a silver photonic crystal array, they surprisingly improved the conductivity of the organic layer, which indicated the significance of the modulation of electromagnetic environment by strong coupling[105]. Beyond the static methods, time resolved transient absorption spectroscopy was also applied by J. C. Owrutsk's group[116] to study strong vibrational coupling in $W(CO)_6$ molecules in a mid-IR cavity, and showed that the relaxation time of vibrational models can be dramatically modified. Later, Wei Xiong's group used two dimensional infrared spectroscopy to reveal the dark state among the polariton states[72]. Besides the above, there are increasing studies in mechanisms and the applications of polaritons in chemical reactions.

In chemistry, one of the most significant processes during chemical reactions is electron transfer. Electron transfer was first proposed by Rudolph A. Marcus in 1956, and further developed as Marcus Theory, which is regarded as the universal model to study the electron transfer kinetics from a donor to an acceptor in the solution. It basically describes how the electron transfer rate can be determined by the free energy difference between reactants

and products, and the reorganization energy. With the assumption of the parabolic potential energy surface in the reaction coordinate, the electron transfer rate reaches the maximum when the free energy difference cancels out the reorganization energy. With the strong coupling of the light in the cavity, the anharmonicity may be introduced into in the potential energy surface, leading to acceleration or suppression of the electron transfer rate, influencing even the pathway or the product selection in the chemical reactions. Therefore, understanding electron transfer has great significance, and the modulation of the electron transfer process by strong coupling has promise for the development of next generation devices.

3.1.2. Purpose and Expectation

Many fundamental questions of chemical reactions under light-matter interaction were studied except for electron transfer. In this project, electron transfer in an optical cavity would be studied as the electron transfer pathway might change with the polariton states. Transient absorption spectroscopy would be the main approach for studying the electron transfer kinetics, and time resolved photoluminescence would provide complementary data.

In principle, a donor and an accepter molecule are needed. At the start of the project, Rhodamine 6G (R6G) molecule was chosen for the cavity fabrication trials, because it is cheap, non-toxic, and it has optical transition around 550 nm. However, R6G was found problematic. A J-aggregate molecule should be more suitable for this project. Due to lack of mature fabrication skills and experience on finding suitable system, here only preliminary results are presented and it is considered as a potential new direction for our group.

3.2. Experiment Methods

3.2.1. Optical Cavity Fabrication

The optical cavity used in this work is Fabry-Perot cavity, which consists of two planar silver mirrors. The fabrication followed Thomas Ebbesen's procedure[64]. Firstly, the R6G molecules were mixed with polyvinyl alcohol in water. Then, a sliver layer was deposited on a cleaned microscope slide, followed by spin-coating a mixture of R6G and PVA with 2000 rpm for 30 sec. After the solution was totally dried and formed plastic layer, another sliver layer was sputtered on the top of the whole film. The completed cavity has the sliver-molecule/polymer-sliver sandwich structure, shown as the diagram in Figure 3.3. The concentration of R6G and PVA is various, depended on the cavity length and resonant condition. All the sliver deposition was performed by thermal evaporation, with kind assistance from Prof. Sergei Urazhdin, in the physics department at Emory University.

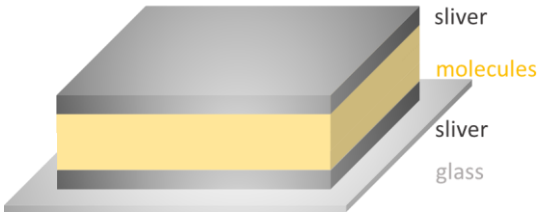

Figure 3.3. Diagram of the sandwich structure molecules in optical cavity.

3.2.2. Transient Absorption Spectroscopy Measurement

The femtosecond pulse beam for transient absorption was provided by a regeneratively amplified 800 nm Ti:Sapphire Laser with 2 mJ pulse energy, 1 kHz repetition rate and 150 fs pulse duration (Legend, Coherent Inc.). Probe beam was formed by white light

generation through pumping around 10 μJ into a sapphire window. The 10% of the white light probe was taken as the reference signal to improve the signal-to-noise ratio. The rest 1.3 mJ of the laser output was used to pump an optical parametric amplifier (Opera, Coherent Inc.), and converted into the signal and idler beam after the second amplification. By combining the sum frequency generation or second order generation of one of these two beams and the fundamental 800 nm beam, a wide range of visible pump beams from400 nm to 750 nm could be obtained. With a synchronized chopper at 500 Hz, the pumped and unpumped absorption spectra were recorded and subtracted. The data acquisition system was a Helios system, from Ultrafast LLC., which captured the signal through a fiber coupled multi-channel spectrometer with a complementary metal oxide semiconductor (CMSO) array. The IRF of the whole setup was estimated about 150 fs by measuring response of toluene in a cuvette. For all the measurement, the probe beam was normally incident.

3.2.3. Time Resolved Fluorescence Measurement

The time resolved fluorescence setup shares the same TCSPC module and excitation laser as already described in previous part. The excitation beam pumped the sample and the transmitted fluorescence photons were collected by an MCP-PMT (Hamamatsu Photonics) after filtering out the excitation beam. For all the measurements, normal incidence was performed.

3.3. Results and Discussion

The physics of Fabry-Perot cavity transmission is given by the follow expression[58, 117-119]:

$$T = \frac{1}{1+(4F^2/\pi^2)sin^2(\phi/2)} \quad \text{eq. (3.2)}$$

where F is the finesse of the cavity, and can be derived by the reflectivity of two parallel mirrors, $R_1$and R_2, as shown in eq. 3.3. ϕ is the phase shift of a round travel of photons the cavity, which is determined by the refractive index n of the medium between two mirrors, the cavity spacing distance L_{cav}, and wavelength of the photons λ, as shown in eq. 3.4.

$$F = \frac{\pi(R_1R_2)^{\frac{1}{4}}}{1-\sqrt{R_1R_2}} \quad \text{eq. (3.3)}$$

$$\phi = 4\pi nL_{cav}/\lambda \quad \text{eq. (3.4)}$$

To begin, the thickness dependent reflectivity of a single sliver mirror on the glass substrate can be estimated by measuring UV-Vis absorption spectrum. Figure 3.4 a shows extinction curves of different thickness of single sliver layer on glass substrate. Here, it was assumed that $T + R \approx 1$. The UV-Vis spectrometer takes transmitted intensity and converts it into absorbance by assuming $T + A \approx 1$. Without molecules, the sliver absorption in visible range is very minor. The thickness of sliver was ranged from 20 nm to 100 nm. When the thickness of silver was 40 nm, the reflectivity of the sliver layer was over 90% (A>1) from 450 nm to 800 nm, which could form high quality cavity. When the sliver layer was thicker, the absorption of the sliver affected the quality of cavity because the strong absorption reduced the reflectivity. Thus, the following cavities were all deposited with 40 nm sliver. In Figure 3.4 b, the resonant cavity mode position could be controlled by tuning concentration of PVA solution. More concentrated PVA solution forms longer spacing distance between two sliver mirrors. The cavity mode position– PVA concentration

relation was estimated by spin-coating 3.5, 4.0, 4.5, and 5.0 wt% PVA solution on a 15 mm × 15 mm glass.

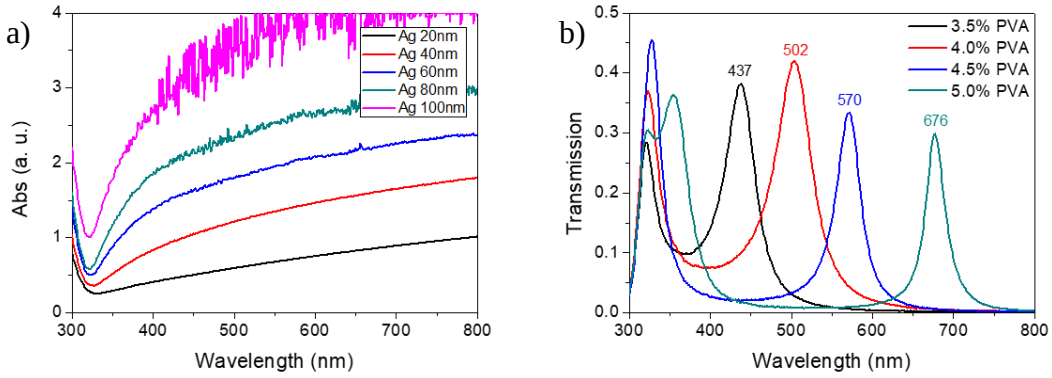

Figure 3.4. a). Extinction curves of different single layer sliver on glass. b) Transmission curves of optical cavity by spin-coating different concentration PVA solution.

As the preliminary trial of studying molecules in optical cavity, J-aggregates, for instance, the TDBC molecule in Thomas Ebbesen's work[64], which formed aggregates with aggregate state dipole moment aligning along with the direction of electric field oscillating within in a two planar mirrors optical cavity, were not involved, considering the price of the molecules. Instead of the J-aggregates, the fluorescence dye R6G was chosen as 1/3 of the transition dipoles that can be coupled with the cavity mode, assuming the orientation of molecular dipoles was randomly distributed. Figure 3.5 a shows the absorption spectrum of R6G in water. The strong exciton transition around 520 nm was the target for the cavity fabrication. According to Figure 3.4 b, 4.0% ~ 4.5% PVA solution was supposed to be used. Thus, a series of concentration of PVA solution from 3.50% to 5.00% were mixed with 5 mM R6G and dispersed in the cavity. The transmission curves were plotted in Figure 3.5 b. When the PVA concentration was around 4.0% to 4.5%, the transmission peak split into two peaks, which indicated the cavity modes were overlapped with R6G transition,

generating two separated polaritonic states and allowing light to pass through. It was a pity that the absorption spectra could not be measured without the integration sphere. However, the splitting proved the strong coupling of R6G molecules in the optical cavity. While PVA solution was too dilute or concentrated, the off-resonance features were displayed, which have an intense peak mainly consisting of the cavity mode and a weak peak mainly consist of the exciton transition[81, 101]. This verified the effectiveness of controlling the cavity mode by tuning concentration of PVA solution. The fluorescence decay of these samples and control samples (R6G in ethanol, R6G in PVA polymer outside of cavity) were measured and plotted in Figure 3.5 c. Except for the free R6G in ethanol, all the other samples' fluorescence decay kinetics showed no clear trend but much faster than the free one. This will be discussed later. For further investigation, the influence of the glass substrate was shown in Figure 3.5 d. All the cavities in Figure 3.5 d were made on 25 mm × 25 mm glass. Although the same concentrated PVA solution was used, all the R6G molecules were not coupled resonantly with cavity. Actually, many other factors might affect the cavity fabrication, and could not considerably be covered. The condition explored in Figure 3.5 b was useful for the further study.

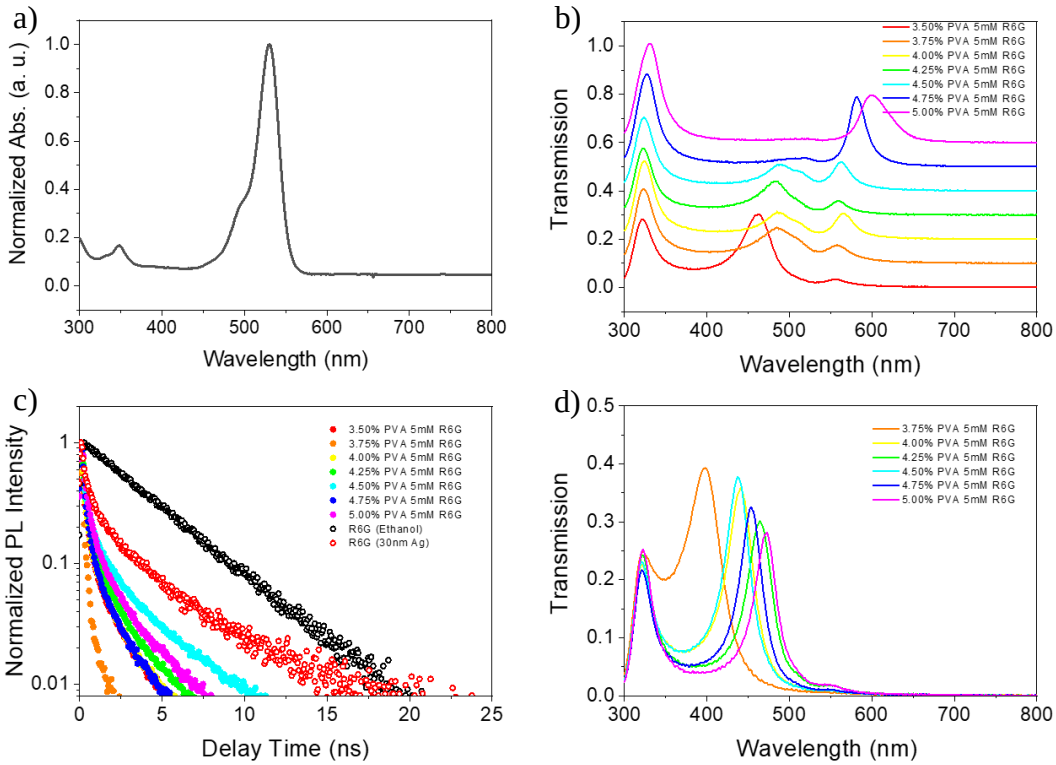

Figure 3.5. a) R6G absorption spectrum in water. b) Transmission curves of 5 mM R6G in optical cavity. The cavity spacing distance was determined by a series of concentrations of PVA solution. c) The PL decay curves of the samples in b). d) Cavities made by 25 mm × 25 mm glass substrate with same conditions as in b). All the samples were off-resonance.

To investigate the relationship between the molecule's density and Rabi splitting, the PVA solution concentration was fixed at 4.50% for strong coupling while the R6G concentration varied. The transmission curves were shown in Figure 3.6 a. For the empty cavity (0 mM R6G), there was no splitting that appeared, although the cavity mode did couple with the R6G transition. With increasing concentrations of R6G molecules, the splitting of the transmission curves was increased. As R6G molecules were distributed randomly in the PVA polymer, the Rabi splitting could be rewritten with a factor of 1/3, and could still be proportional to the sqrt of the molecular density. Since the volume of the cavity was fixed,

the relation between Rabi splitting and the square root of the molecular concentration was plotted in Figure 3.6 b. Due to the limitation of the fabricated cavity, the precise cavity mode could not be reproduced very well, thus the cavity mode when containing molecules or not might be quite different. The transmission curves were not able to be fitted. The Rabi splitting could only be estimated by subtracting the two transmission peaks energy levels. Even though, the Rabi splitting roughly kept the linear relationship with the square root of the concentration, which could be reflected as the red dashed line inFigure 3.6 b.

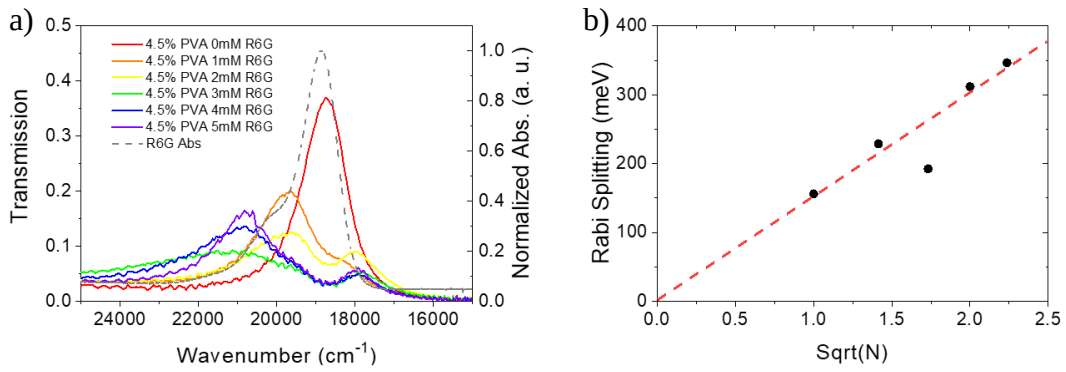

Figure 3.6. a) Optical cavities fabricated with 4.5% PVA solution and various concentrations of R6G from empty cavity to 5 mM. b) Linear relationship between Rabi splitting and sqrt of R6G concentration.

It has been reported strong coupling can alter the lifetime of excited states. To study the excited state dynamics, TAS is applied. The transient absorption spectra of the sample series of Figure 3.5. b were presented in Figure 3.7 with excitation of upper polariton band (P+) at 500 nm and lower polariton band (P-) at 550 nm. Both polariton bands showed ground state bleach peaks, and the subtracted spectra shapes varied with the concentration of the PVA solution. Compared with the TAS of the R6G molecules in PVA polymers outside of the cavity in Figure 3.8 a, and free R6G molecules in ethanol in Figure 3.8 b, it

is quite clear that whether the R6G molecules were inside or outside of the cavity, as long as R6G molecules were trapped in PVA polymers, the ground state bleach signal decays extremely quickly within 100 ps. The exciton lifetime of free R6G molecules in ethanol is about 4 ns. This mismatch is due to the dimerization of the concentrated R6G in polymer[120]. As R6G/PVA/water solution was spin-coated on the glass substrate, a majority of the water was evaporated during dry casting. The rest of the water was involved in polymerization which significantly increased the concentration of R6G in the plastic polymer. The formation of R6G dimer traps the exciton formed by monomer, causing the fast decay of R6G in polymer film. In principle, R6G is not a good molecule to study strong coupling issue.

The transient absorption spectra can be attributed analytically by the transmission curves of a cavity containing medium with certain amount of excited stated population [72, 75, 88, 116, 121-124]:

$$T_{cav}(\bar{\nu}) = \frac{T^2 e^{-\alpha L_{cav}}}{1+R^2 e^{-2\alpha L_{cav}} - R e^{-\alpha L_{cav}} \cos(4\pi n L_{cav} \bar{\nu} + 2\varphi)} \quad \text{eq. (3.3)}$$

where α accounts for the exciton coefficient of the molecules in the cavity, and n represents the wavenumber dependent refractive index. φ denotes the phase shift as light reflects at the mirror. To obtain the n and α, the dielectric function of real ε_1 and imaginary ε_2 part of the cavity medium was derived with a format of sum of Lorentzian functions:

$$\varepsilon_1 = n_{bg}^2 + \sum_i \frac{A_i(\nu_i^2 - \nu^2)}{(\nu_i^2 - \nu^2)^2 + (\Gamma_i \nu)^2} \quad \text{eq. (3.4)}$$

$$\varepsilon_2 = \sum_i \frac{A_i \Gamma_i \nu}{(\nu_i^2 - \nu^2)^2 + (\Gamma_i \nu)^2} \quad \text{eq. (3.5)}$$

Where n_{bg} is the background medium refractive index, and A_i, ν_i, Γ_i represent the amplitude, resonant frequency, linewidth of the i^{th} mode, respectively. With ε_1 and ε_2, the n and α can be derived as:

$$n = \sqrt{\frac{\varepsilon_1 + \sqrt{\varepsilon_1^2 + \varepsilon_2^2}}{2}} \qquad \text{eq. (3.6)}$$

$$\alpha = 4\pi\nu\sqrt{\frac{-\varepsilon_1 + \sqrt{\varepsilon_1^2 + \varepsilon_2^2}}{2}} \qquad \text{eq. (3.7)}$$

In fact, even if the theoretical knowledge is sufficient, R6G was not a good system, as the dimerization made the analysis much more sophisticated. Another serious issue was that the reproducibility was poor for this fabrication method. The cavity modes could be duplicated with the same condition easily, but the thermal evaporation could not always produce the same sliver thickness. These obstacles made some important parameters unmeasurable nor reliable based on assumption. In addition, a molecular system with donor and acceptor was not familiar to us, as dimerization might be a very common issue in a concentrated condition.

Nanocrystal systems were also explored, such as QDs or semiconductors in the optical cavity, but strong coupling was never achieved in this project. While the nanocrystals are one hundred times larger than molecules, the large-size induced surface roughness caused trouble when depositing sliver layer. The sliver layer always looked cloudy but not mirror-like, which had much lower reflectivity. Furthermore, larger size dramatically reduced the concentration, which might impede the light-matter interaction move forwards to the strong coupling regime. As most literature in this field only reported strong coupling of QDs in

nano photonic array, the charge transfer between QDs and molecules in strong coupling condition is still a very interesting topic.

3.4. Conclusion

The project was terminated due to lack of experience in the field and poor fabrication reproducibility. Fortunately, strong coupling between R6G molecules in two planar silver mirrors was investigated by static transmission measurement. We found the splitting of the energy levels scales with the sqrt of the R6G concentration. However, due to the formation of dimer, the intrinsic exciton lifetime has been altered. Thus, time resolved fluorescence measurement and transient absorption spectroscopy measurement fail to offer further information on how cavity would modify the carrier dynamics. However, this preliminary result should still be helpful for accumulating the knowledge of light-matter interaction for further study in the future.

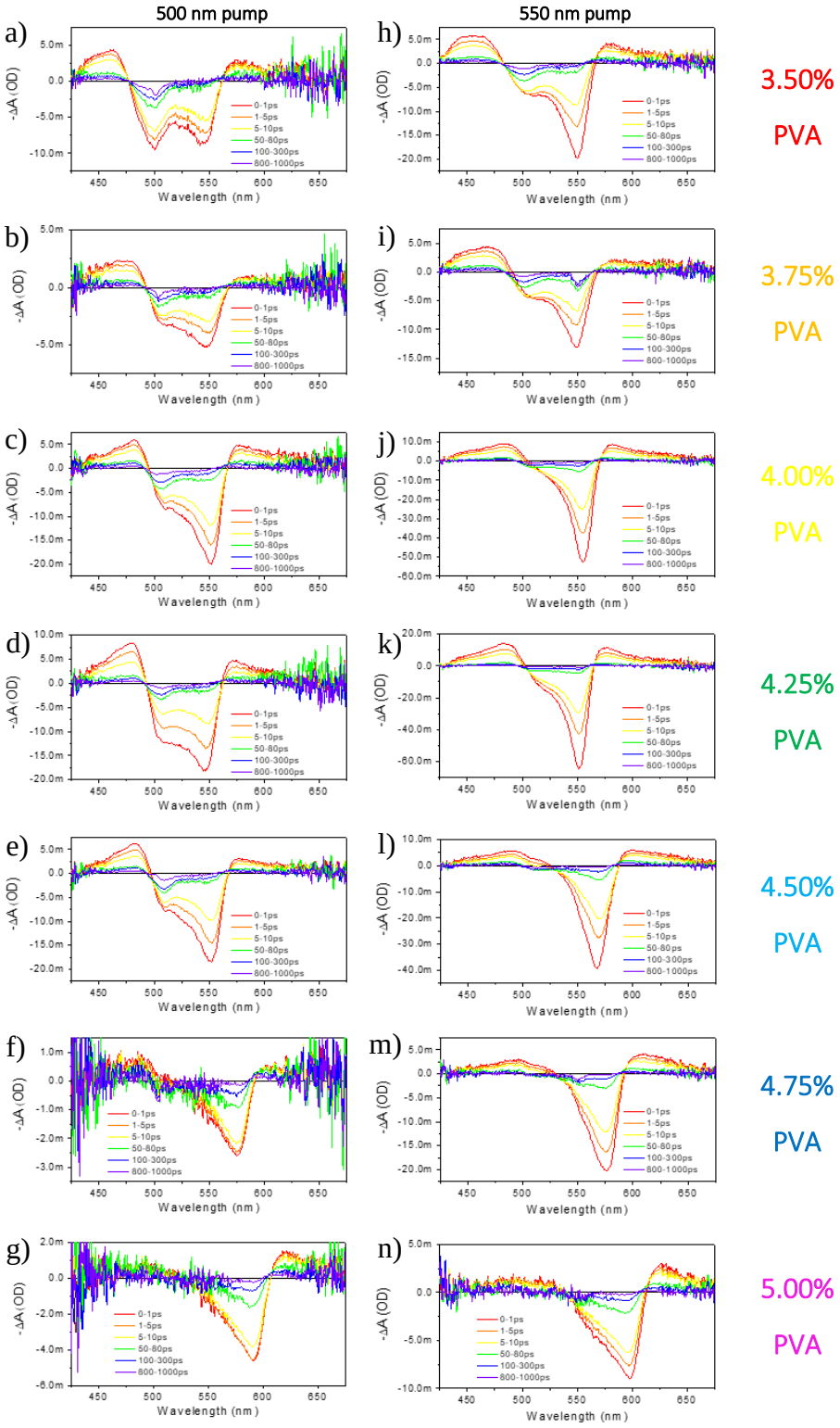

Figure 3.7 TAS of the R6G in cavities. a), b), c), d), e), f), g) 500 nm pump; h), i), j), k), l), m), n) 550 nm pump. The spectral shape changed with the shift of cavity transmission.

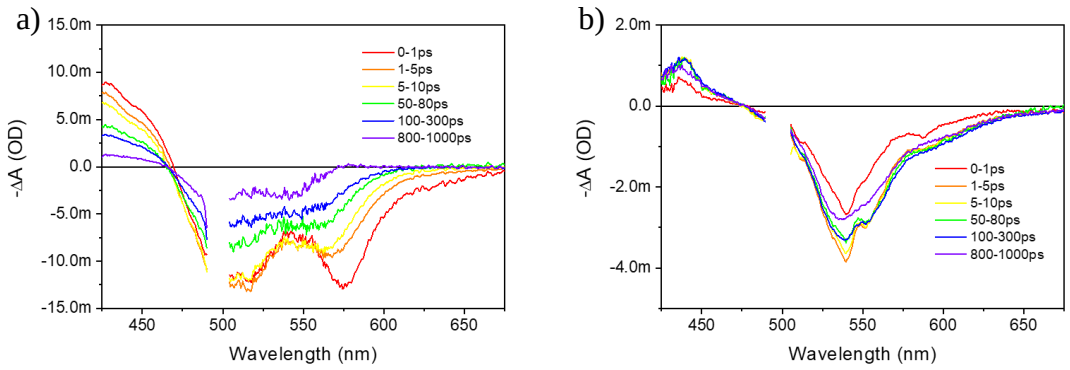

Figure 3.8 a) TAS of R6G molecules in 4.5% PVA polymers film outside of the cavity, pumped by 500 nm. b) TAS of free R6G molecules in ethanol, pumped by 500 nm.

4. Investigation of A Novel Rhenium Disulfide Electrocatalyst by Vibrational Sum Frequency Generation Spectroscopy

4.1. Introduction

Heterogeneous electrocatalysis has been developed as a promising approach to overcome the energy regeneration issues around the world. This field has made progress in the enhancement of stability, selectivity, and productivity of the catalytic reaction, especially in electrocatalytic reactions. By binding electrocatalytic molecules onto a metal or semiconductor electrode surface, CO_2 reduction or H_2 evolution can be more efficient. However, the behaviors of catalysts during heterogeneous electrocatalysis have always been of interest, particularly in understanding how the interfacial electric field interacts with molecules. In this paper, a novel rhenium-based CO_2 reduction electrocatalyst $Re(SSbpy)(CO)_3Cl$ was synthesized and attached to polycrystalline gold film electrode. By probing the symmetric CO stretching mode with potential dependent SFG vibrational spectroscopy, the Stark shift rate of 7~8 $cm^{-1}V^{-1}$ under applied bias was revealed, indicating a weak correlation between the symmetric CO stretching dipole and the interfacial electric field. In addition, DFT calculations indicated that this molecule tended to be adsorbed on the gold surface with a nearly zero tilt angle with great agreement to spectroscopic results.

4.1.1. Background

CO_2 reduction has extraordinary significance in solving the problem of energy consumption and sustainability in future prospects. The emission waste and greenhouse gas can convert into regenerative fuels through the CO_2 reduction reaction[125-126]. Electrochemical catalytic CO_2 reduction reaction has fascinated scientists' focus because of its great potential however, the difficulty of improvement of stability[127-129], selectivity[130-133], and efficiency[134-136] are still the most challenging issues all around the world.

To overcome these barriers, a homogeneous catalyst $Re(bpy)(CO)_3Cl$ and its derivatives were synthesized and reported as a series of CO_2 selective and highly efficient electrocatalysts with low onset potential to reduce CO_2 to CO, in 1984[137]. Recently, heterogeneous catalysis, through immobilizing catalysts on a metal or semiconductor surface, is developing promisingly. Compared with homogeneous catalysis, heterogeneous catalysis can be more easily recycled and achieve greater catalytic selectivity[138-139], but it brings difficulties on characterization of the catalysts. Many molecular behaviors and responses at the interface of surface and solution are thereby not understood unambiguously, particularly the catalytic mechanism affected by the interfacial electric field[140-141]. With regard to the detection of molecules attached on the surface during the electrochemistry reaction, in-situ electrochemical sum frequency generation vibrational spectroscopy offers its unique benefits to exclusively probe the vibrational mode of the catalysts adsorbed on the electrode surface over a potential range[142-144]. Due to the nature of the second order nonlinear response, only the interface between the solid electrode and solution can generate an asymmetric electronic environment[145]. Therefore, electrochemical SFG is believed to be a powerful tool to study the interfacial chemical reaction between

catalyst and redox couples. SFG can also offer insights in how interfacial electric field would impact the reactions.

A novel rhenium bipyridine tri-carbonyl chloride catalyst with a disulfide bond on the bipyridine ring was recently synthesized. The significant interest for the disulfide bond modification is that the bond will break and form two Au-S bonds when binding on the gold electrode surface. With knowledge of the previous Re complexes, to study this catalyst molecule with a new type of binding structure by electrochemical SFG will expand the understanding of the electrochemical interface and catalysis, which may even help improve the guidance of the catalyst design.

4.1.2. Purpose and Expectation

In this work, the interfacial electric field induced Stark tuning of $Re(SSbpy)(CO)_3Cl$ was investigated by scanning SFG vibrational spectra with different applied bias. Beyond the spectroscopic results, DFT calculations was also conducted to predict the orientation and states of the catalyst at different potentials. By the integration of experimental data with a theoretical model, we reported the response of $Re(SSbpy)(CO)_3Cl$ to the interfacial electric field under different potentials.

4.2. Experiment Methods

4.2.1. SFG Measurements

The experimental setup of SFG spectroscopy is shown in Figure 4.1. A commercial Yb: KGW laser (CARBIDE, Light Conversion, Ltd.) provides a ~290 fs ultrafast pulse beam

at 1030 nm with a 200 μJ per pulse. 90% of the output is firstly compressed and then enters the high power optical parametric amplifier (Orpheus-HP, Light Conversion, Ltd.) to generate a broadband mid-infrared pulse from 1350 nm to 16000 nm. The other 10% of uncompressed 1030 nm output is directly introduced into the second harmonic band compressor (SHBC, Light Conversion, Ltd.), in which two inversely chirped pulses with the same magnitude are modulated from the broadband 1030 nm pulse and generate a narrowband 515 nm pulse with ~6 cm^{-1} bandwidth by neutralizing the opposite temporal chirp during second harmonic generation in a BBO crystal. An integrated acoustic-optical modulator could tune the pulse repetition rate up to 200 kHz.

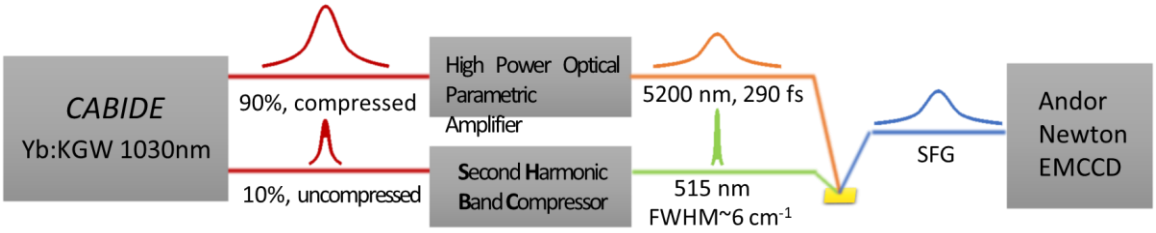

Figure 4.1. Experimental setup scheme of high repetition rate sum frequency generation spectroscopy.

For the SFG measurement geometry, a narrowband *p*-polarized VIS pulse at 515 nm and a broadband *p*-polarized IR pulse centered at 5150 nm were focused on the gold film electrode with the angle of incidence as 65° and 40° respectively. The reflected *p*-polarized SFG signal was collected by Shamrock S500i spectrometer with its combined Newton EMCCD (Andor Technology, Ltd.).

For the phase-sensitive SFG measurement, the angle of incidence of the IR pulse at the first sample stage was set to 55°. The reflected SFG, VIS and IR were again focused onto

the second sample stage by a parabolic mirror. Finally, the phase-sensitive SFG signal was imaged into the detector.

The SFG signal and imaginary part can be described with the following expressions[143-144, 146-149]:

$$I_{SFG} \propto \left| A_{NR} e^{i\varphi} + \sum_q \frac{A_q}{\omega_{IR} - \omega_q + i\Gamma_q} \right|^2 I_{VIS} I_{IR} \qquad \textbf{eq}.\ (4.1)$$

$$Im\left[A_{NR} e^{i\varphi} + \sum_q \frac{A_q}{\omega_{IR} - \omega_q + i\Gamma_q} \right] = A_{NR} \sin\varphi - \sum_q \frac{A_q \Gamma_q}{(\omega_{IR} - \omega_q)^2 + {\Gamma_q}^2} \qquad \textbf{eq}.\ (4.2)$$

where A_q, ω_q, and Γ_q respectively represent amplitude, frequency and dephasing time of the q th mode. A_{NR} indicates the amplitude of non-resonant signal, which comes from the substrate SFG response, and φ means the relative phase difference between the non-resonant signal and resonant signal.

4.2.2. Orientation Extraction from SFG Spectra

Orientation information of molecules can be extracted from SFG spectra though the second order hyperpolarizabilities $\beta^{(2)}_{ijk,q}$, as described in many previous literatures[143-144, 146, 150-151]. The second order susceptibility of the interface composed of molecules can be defined in terms of $\beta^{(2)}_{ijk,q}$ as:

$$\chi^{(2)}_{IJK,q} = \sum_{ijk} \langle (\hat{I} \cdot \hat{\imath})(\hat{J} \cdot \hat{\jmath})(\hat{K} \cdot \hat{k}) \rangle \beta^{(2)}_{ijk} \qquad \textbf{eq}.\ (4.3)$$

in which the molecular coordinators are converted to the laboratory coordinators by ZYZ Euler rotation. The second order susceptibility of *ppp* polarization combination $\chi^{(2)}_{ppp,q}$ can be derived as:

$$\chi^{(2)}_{ppp,q} = -L_{xxz}\chi^{(2)}_{xxz,q} - L_{xzx}\chi^{(2)}_{xzx,q} + L_{zxx}\chi^{(2)}_{zxx,q} + L_{zzz}\chi^{(2)}_{zzz,q} \qquad \textbf{eq}.\ (4.4)$$

where L_{ijk} indicates the Fresnel factors, and they are listed in Table 4.1[143].

Table 4.1. Fresnel Factors of homodyne (IR AOI = 40°) and heterodyne (IR AOI = 55°) SFG.

	IR AOI=40°	**IR AOI=55°**
$\|L_{zxx}\|$	0.14	0.18
$\|L_{xzx}\|$	0.03	0.03
$\|L_{xxz}\|$	0.19	0.02
$\|L_{zzz}\|$	1.06	1.35

Molecular orientation information can be extracted from SFG spectra by mapping out the tilt (θ) and twist (ψ) angles by DFT calculation and searching the combination which matches the experimental spectra best. This work is leaded by Prof. Batista group at Yale University, and it is still ongoing.

4.2.3. SAM Preparation

Polycrystalline gold film electrodes were prepared from microscope slides coated by 100 nm Au and 7.5 nm Cr as the adhesive layer, which were purchased from Substrata Thin Film Solutions, Inc. The gold films were firstly pretreated in an ultrasonic bath in acetone for 5 min, and then in ethanol for 5 min. The above step was repeated once again before drying with nitrogen flow. The cleaned gold films were immersed in 1mM ReSS/DMF solution for over 48 hours for ReSS assembled as a monolayer at the gold film surface. Before SFG measurements, the gold films were rinsed and washed by ethanol three times, and then stilly dried in air. Electrolyte was made by mixing 10 mM sodium hydroxide with Milli-Q water. The NaOH solution was bubbled with nitrogen for 30 min, prior to electrochemistry SFG measurement.

4.2.4. Electrochemical SFG Measurements

The electrochemical SFG setup was modified from our previous ideas[143-144]. As shown in Figure 4.2, the electrochemical SFG was run in a chamber electrochemistry cell. A glass dish which served as electrolyte container was placed in a sealed clear plastic box. The gold film attached with copper tape was fixed in the glass dish as the working electrode. The adhesion part of the gold film and the copper tape was covered by epoxy resin for isolation. A 2 mm CaF_2 window was pressed on the gold film as cell window. To control the thickness of the electrolyte solution, 50 μm PTFE spacers were added between gold film electrode and CaF_2 window. A Pt wire counter electrode was cleaned by flame baking in advance. At the beginning of the in-situ electrochemical SFG measurement, purging plastic chamber with nitrogen flow for 15 min was followed by injection of nitrogen bubbled NaOH electrolyte. The chamber was continuously purged with gentle nitrogen flow during the electrochemical SFG scans.

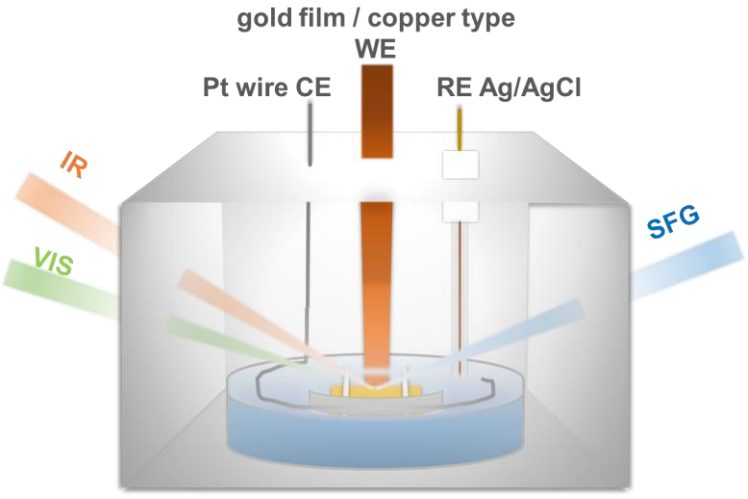

Figure 4.2. Diagram of electrochemical SFG in chamber cell geometry.

A potentiostat (CH Instruments, Inc.) controlled the potential from +0.30 V to -1.10 V vs. Ag/AgCl (1M KCl) with scan rate of 2 mV/s. After several cycles of electrochemical SFG scans, the SAM was removed from the gold film surface by adding -1.60 V for 50 sec. Afterward, the SFG spectrum of the nearly bare gold film was collected for normalization of IR spectral shape. For the balance of the SAM photostability and SFG signal quality, each spectrum was integrated for 25 sec with the pulse repetition rate at 10 kHz. All the involved SFG signals were with the *ppp*-polarization combination.

4.2.5. Impedance-Potential Measurements

The capacitance was measured in a glass beaker with PTFE cap. The ReSS adsorbed gold film slides were immersed into 10 mM NaOH/H_2O solution with approximate area of 1 cm × 0.8 cm. The impedance-potential measurement was performed under 100 Hz, 5 mV AC voltage. The applied potential scanned with 5 mv/s from +0.30 V to -0.90 V vs. Ag/AgCl (1M KCl) and then backward. The electrolyte was bubbled by nitrogen flow in advance. The total capacitance of a SAM modified gold film electrode can be determined as[152-154]:

$$\frac{1}{C_{total}} = \frac{1}{C_{SAM}} + \frac{1}{C_{GC}} \qquad \textbf{eq}.\ (4.5)$$

where C_{SAM} and C_{GC} represent capacitance induced by the SAM and diffuse layer respectively. Both C_{SAM} and C_{GC} change at different applied potentials while C_{GC} dominates. In this case, the minimum of the capacitance-potential curves can be used to estimate the potential of zero charge.

4.2.6. Sample Information

The catalyst $Re(SSbpy)(CO)_3Cl$ was synthesized by our collaborator Mauricio Cattaneo from Universidad Nacional de Tucumán. The molecule structure and spectroscopic characterization are shown in Figure 4.3 a, b and c.

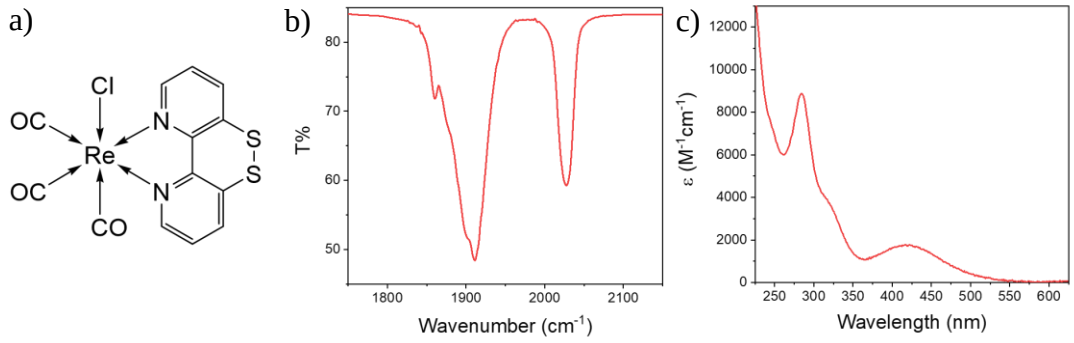

Figure 4.3. a) $Re(SSbpy)(CO)_3Cl$ molecule structure. b) FTIR spectrum of ReSS in KBr pellet. c) UV-Vis absorption spectrum of ReSS in acetonitrile.

4.3. Results and Discussion

4.3.1. Homodyne and Heterodyne SFG Spectrum of ReSS SAM in Air

The common SFG and phase sensitive SFG of $Re(SSbpy)(CO)Cl_3$ SAM at gold film were measured in air (Figure 4.4 a). As shown in top of Figure 4.4 b, the SFG spectrum of ReSS shows a pronouced CO symmetric stretching mode around 2030 cm^{-1}. Besides this, it also exhibits a shoulder at lower frequnecy region around 1950 cm^{-1}, which probably could be assigned to CO asymmetric stretching mode. The resonant mode of the SFG signal was fitted and showed the frequency of the CO stretching mode at 2026 cm^{-1}. Due to ambiguity of the low frequency mode, phase-sensitive SFG was performed and the result was plotted in the bottom of Figure 4.4 b. Through the expression of the imaginary part of SFG signal, the extremum usually indicates the frequency of resonant mode. The SFG spectrum shows a huge amplitude of the CO symmetric stretching mode and a noise-level amplitude of the CO asymmetric stretching mode. Understanding the orientation of the catalyst on the

surface has significant meaning to visualize the interfacial reaction. Orientations of the catalyst may alter its reactivity and may also affect the reaction selectivity through interfacial bonding or steric effects. From the ratio of amplitudes from these two peaks, the orientation of ReSS SAM can be implied. Taking the direction of the CO symmetric and asymmetric dipole moments into consideration, only the situation that the ReSS nearly stands up vertically at gold surface matches the best. The dipole of the CO symmetric stretching mode can couple with *p* polarized infrared beam, resulting in huge amplitude , while the dipole of CO asymmetric mode is almost parallel to the gold surface, thus, resulting in negeligible signal amplitude.

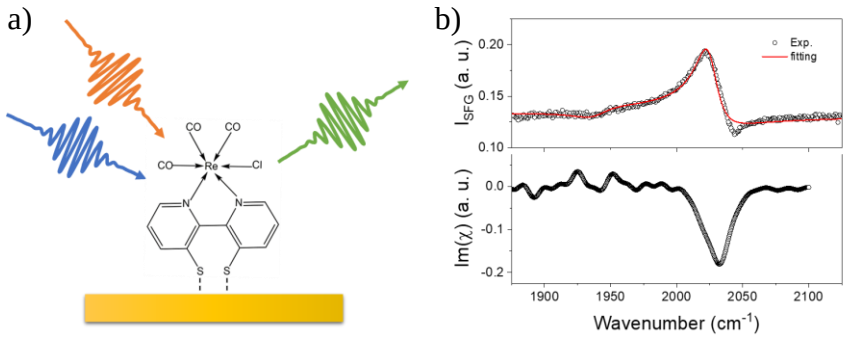

Figure 4.4. a) Scheme of SFG measurement in the air. b) homodyne SFG spectrum with fitting result (top) and heterodyne SFG spectrum (bottom).

Further analysis will be performed by our collaborators via computational simulation. By scanning the configurations of tilt (θ) and twist (ψ) angles in DFT optimization, the best matched simulated spectrum can be found and the orientation of the ReSS at gold films can be defined.

4.3.2. Electrochemical Vibrational Stark Shift

To investigate the influence of the electric field at the interface of the gold film and electrolyte on the SAM of ReSS, SFG spectrum were scanned synchronously with cyclic

voltammetry. To avoid irreversible dissociation of ReSS from gold surface and suppress hydrogen evolution in the negative potential regime[143], the potential range was set from +0.30 V to -1.10 V. Meanwhile, 10 mM NaOH was selected to offer a base environment and conductivity while more concentrated base electrolyte would promote the irreversible desorption process[143].

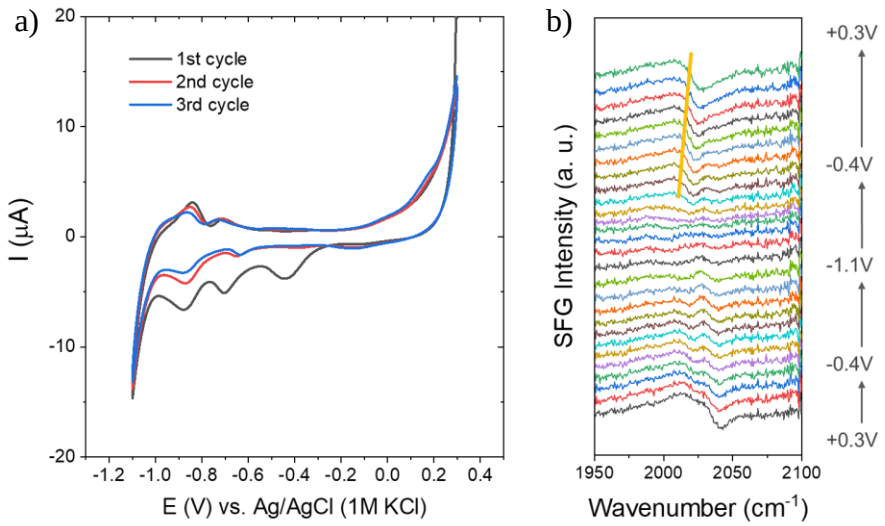

Figure 4.5. a) Cyclic voltammogram associated with potential dependent SFG scans. b) First cycle potential dependent SFG scans.

The cyclic voltammogram of three successive cycles of the potential-dependent SFG measurement was shown in Figure 4.5 a. In the initial negative sweep of the first cycle, multiple reductive peaks appeared respectively at -0.44 V, -0.70 V and -0.88 V, as well as the large cathodic current that started flowing at -0.24 V. The reductive peak at -0.44 V and -0.70 V during the cathodic current disappeared in the following cycles. Although these reductive peaks and current are still ambiguous, they could be attributed to electrochemical surface equilibrium, probably due to disordered ReSS molecules outside of SAM or

contamination induced adsorption/desorption. In the both of the following two cycles (Figure 4.6 a and d), two reductive desorption peaks occurred at -0.64 V and -0.87 V. According to the previous study of $Re(bpy)(CO)_3Cl$ with a functional thiol group[155-158], the disulfide bond could break with the formation of two Au-S bonds when self-assembled at the gold surface. Therefore, these two peaks can be assigned to the desorption of two Au-S bonds one after another. The current increased crucially while the hydrogen evolution reaction just started at -1.00 V. Correspondingly, there were two re-adsorption peaks at -0.85 V and -0.73 V, during the positive going sweep. It is remarkable that the CV curves were reproducible except that the current ampiltude was weaker after each cycle. Compared with desorption peaks, the adsorption peaks in the same cycle always had less amplitude, indicating that some ReSS was dissociated from the gold surface into the solution.

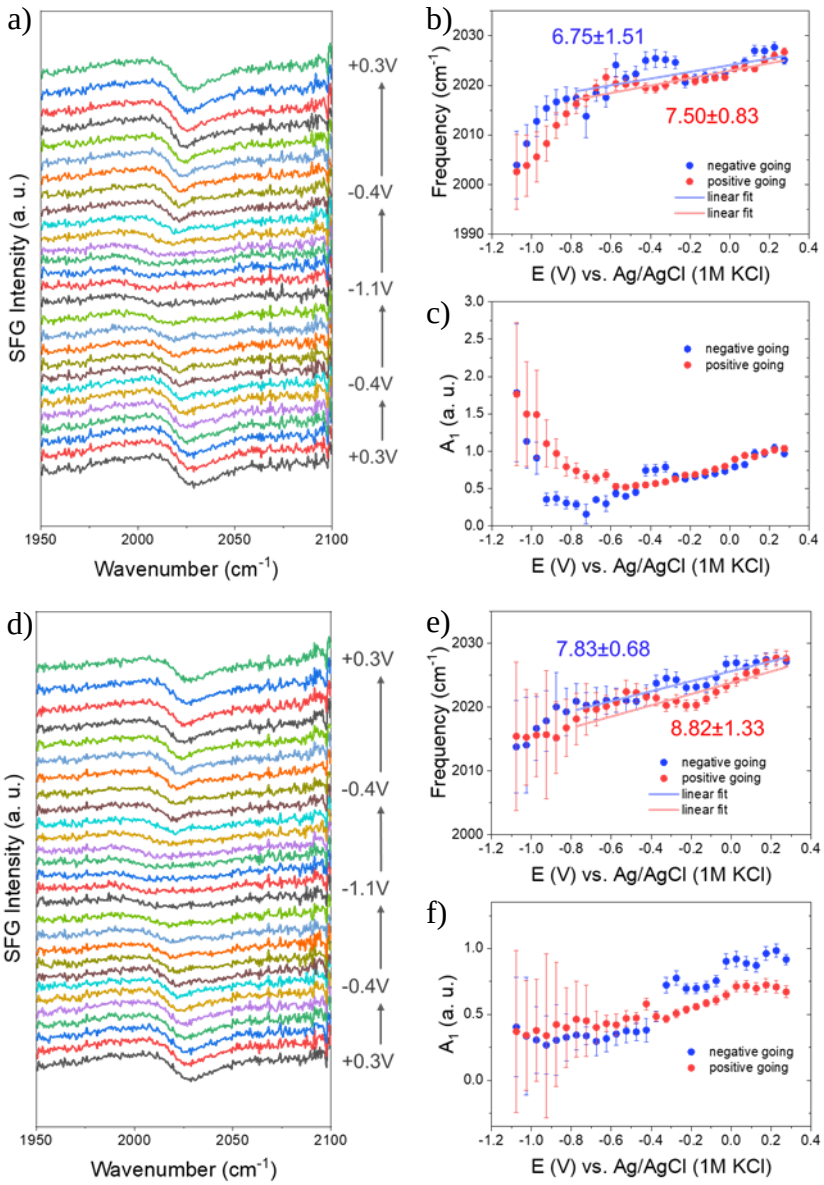

Figure 4.6. a), b) and c) are spectra, frequency and amplitude fitting results of second cycle potential dependent SFG respectively. d), e) and f) are spectra, frequency and amplitude fitting results of second cycle potential dependent SFG respectively.

Corresponding to the CV curves, three successive cycles of the SFG spectra with different bias were plotted in Figure 4.5 b (1st cycle), Figure 4.6 a (2nd cycle) and Figure 4.6 d (3rd

cycle). The SFG scans with different potential were offset for clarity. The symmetric C≡O stretching mode of ReSS was probed while the asymmetric C≡O stretching mode was barely observed. This is consistent with the theoretical configuration model which predicts that ReSS would stand erect on the gold surface; thus, the transition dipole of the symmetric C≡O stretching mode has a vertical component to the surface while the dipole of asymmetric C≡O stretching mode is nearly parallel to the substrate. Overall, the SFG spectra changed in an apparently different way during the negative going sweep of the first cycle, while the changes of SFG spectra appears in a similar way in the following cycles (details show the comparison of shapes of the certain specific spectrum). The frequency of the C≡O stretching mode decreases in the negative going sweep and increases backward in the positive going sweep after surface equilibrium. Besides, the amplitude of the ReSS signal almost disappeared at around -1.10 V, indicating that the ReSS molecules desorbs from the gold surface and are totally dispersed in the solution. The stability and reproducibility were tested with another separate control sample using the same experimental conditions with more successive scans. The trend of frequency shifting was consistent while the initial amplitude of ReSS signal at the beginning of each cycle dropped gradually. This supports the irreversible dissociation of ReSS in CV curves.

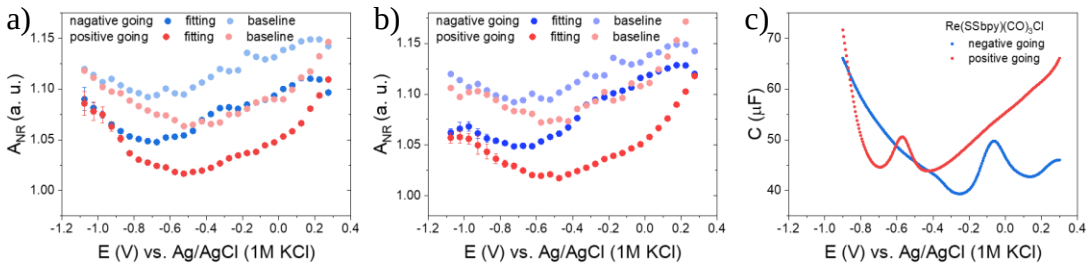

Figure 4.7. a) Fitting results of non-resonant signal in 2nd cycle of electrochemical SFG scans. b) Fitting results of non-resonant signal in 3rd cycle of electrochemical SFG scans. c) Capacitance-potential curves.

To further understand the interfacial electric field induced frequency shift of ReSS CO stretching mode, potential dependent SFG spectra of the second (Figure 4.6 a) cycle were fitted with a normalized SFG signal formula. The frequency and amplitude of the symmetric CO stretching mode were plotted in Figure 4.6 b and c respectively. During the Stark tuning of the CO stretching mode with respect to different applied potentials, the frequency of the CO mode shifts gradually to lower wavenumbers in the cathodic sweep and shifts backward in the anodic sweep. Notably, the frequency shifting rate changed suddenly around -0.80 V, where the first Au-S bond had already dissociated and the reductive current of second Au-S bond was about to flow. Consistently, the amplitude of the CO mode dropped steadily between +0.30 V and -0.80 V and became intricate at a more negative potential. Herein, the complexity of the determination of the amplitude originates from the peak width broadening and amplitude decrease. The Stark tuning rate of CO stretching mode between +0.30 V to -0.80 V extracted through linear fitting was 6.75±1.51 cm^{-1}/V in the negative going sweep, and 7.50±0.83 cm^{-1}/V in the positive sweep. A previous study[143] of a similar rhenium based catalyst, Re(S-2,2'-bpy)$(CO)_3$Cl showed the Stark tuning rate at the polycrystalline gold surface is 21.0±2.0 cm^{-1}/V. The DFT calculation results of Re(S-2,2'-bpy)$(CO)_3$Cl demonstrated that the optimal tilt angle is 65°~75°, depending on whether the CO or Cl faces the gold surface. This significant difference indicates that the CO groups of Re(SSbpy)$(CO)_3$Cl should be located farther away from the gold surface than the CO groups of Re(S-2,2'-bpy)$(CO)_3$Cl, consequently,

the former CO mode frequency shifts slower under weaker interfacial electric field while the latter CO mode frequency shifts faster under stronger interfacial electric field. Furthermore, this result concurrently agrees with the vertical adsorption model from DFT predictions. Likewise, the spectra of the third cycle of electrochemical SFG scans were also analyzed and plotted in Figure 4.6 d, e and f. The Stark tuning rate of the CO mode in the negative going sweep and positive going sweep was 7.83±0.86 cm^{-1}/V and 8.82±1.33 cm^{-1}/V respectively. According to other fitting results, the trend of frequency shifting and amplitude variation under bias follows quite well with the second cycle, which verifies the reproducibility and stability.

Additionally, the non-resonant signal of the 2nd and 3rd cycle scans of potential dependent SFG measurements was plotted in Figure 4.7 a and b. The dark dots and the light dots indicated the non-resonant signal amplitude extracted from fitting results and averaging of spectra signal between 2075 cm^{-1} and 2085 cm^{-1}, respectively. Both series of dots in negative going sweep demonstrated minima around -0.70 V, while the minima occurred at about -0.50 V during the positive going sweep. The displacement between dark and light dots was caused by the baseline slopes in the spectra. As the previous study reported[159-163], the minimum signal of second order nonlinear spectroscopy is dominated by the contribution from the susceptibility of the substrate ($\chi_{Au}^{(2)}$), which indicates the interfacial electric field induced third order nonlinear response ($\chi^{(3)}\Delta\Phi, \Delta\Phi = Eapplied - EPZC$) reaches the minimum in this case. These non-resonant signal minima could be attributed to the cancellation of the static electric interaction between the gold and solution interface, that is to say, the applied potential at this moment is equivalent to potential of zero charge. According to the impedance-potential measurement results shown in Figure 4.7 c, the

minima of capacitance in both negative and positive going sweeps were roughly around 0.40 V, which follows the fitting results of electrochemical SFG spectra and alkanethiol modified gold surface reported by other literatures[164-166].

4.4. Conclusion

The CO_2 reduction catalyst $Re(SSbpy)(CO)_3Cl$ was characterized by SFG spectroscopy. Through electrochemical SFG vibrational spectroscopy, the interfacial electric field induced Stark shifting of the symmetric CO mode was investigated in the potential region from +0.30 V to -1.10 V. Combined with DFT calculations, the ReSS was estimated to stand almost perpendicularly to the gold surface, which proposed a comprehensive model for the study of heterogeneous electrocatalysts in the further future.

5. Summary

The projects presented in this thesis comprehensively demonstrate the application of ultrafast laser techniques in physical chemistry scientific research. Ultrafast and nonlinear spectroscopies can be also applied to many aspects in other fields. Time resolved photoluminescence can offer the information of fluorescence lifetime and decay pathway. Combined with an AFM, single-molecule level detection of the time-domain fluorescence spectroscopy was applied to study single particle fluorescence quenching, decreasing the complexity of modeling and simulating in an ensemble system. Transient absorption spectroscopy has widespread applications in the study of exciton and carrier dynamics. Using transient absorption spectroscopy to study polariton dynamics has shown promise. To investigate the heterogeneous CO_2 catalyst response at interfaces, sum frequency generation spectroscopy was developed and performed. Modeling of a similar catalyst under bias also contributed to this study.

This thesis is a great opportunity to summarize these advanced ultrafast techniques involved in my projects, and my contribution for further development of these techniques. Despite certain difficulties that cannot be overcome in these experiments, other physical chemists should take advantage of these sophisticated technologies for deeper and more comprehensive research. Generally, ultrafast laser techniques have always had strong potential for providing new knowledge and hold a significant position in scientific research.

6. Reference

1. Becker, W., *Advanced time-correlated single photon counting applications*. Springer: 2015; Vol. 111.
2. Wahl, M., Time-correlated single photon counting. *Technical Note* **2014**, 1-14.
3. Becker, W., The bh TCSPC Handbook, Fifth Edition **2012**.
4. Hamamatsu, K., Photomultiplier Tubes. Basics and Applications. *Edition 3a* **2006**.
5. Hunt, J. H.; Guyot-Sionnest, P.; Shen, Y. R., Observation of C-H stretch vibrations of monolayers of molecules optical sum-frequency generation. *Chemical Physics Letters* **1987,** *133* (3), 189-192.
6. Choi, J.-s.; Jun, Y.-w.; Yeon, S.-I.; Kim, H. C.; Shin, J.-S.; Cheon, J., Biocompatible heterostructured nanoparticles for multimodal biological detection. *Journal of the American Chemical Society* **2006,** *128* (50), 15982-15983.
7. Wu, K.; Zhu, H.; Liu, Z.; Rodríguez-Córdoba, W.; Lian, T., Ultrafast Charge Separation and Long-Lived Charge Separated State in Photocatalytic CdS–Pt Nanorod Heterostructures. *Journal of the American Chemical Society* **2012,** *134* (25), 10337-10340.
8. Wu, K.; Chen, Z.; Lv, H.; Zhu, H.; Hill, C. L.; Lian, T., Hole Removal Rate Limits Photodriven H2 Generation Efficiency in CdS-Pt and CdSe/CdS-Pt Semiconductor Nanorod–Metal Tip Heterostructures. *Journal of the American Chemical Society* **2014,** *136* (21), 7708-7716.
9. Wu, K.; Zhu, H.; Lian, T., Ultrafast Exciton Dynamics and Light-Driven H2 Evolution in Colloidal Semiconductor Nanorods and Pt-Tipped Nanorods. *Accounts of Chemical Research* **2015,** *48* (3), 851-859.
10. Wu, K.; Lian, T., Quantum confined colloidal nanorod heterostructures for solar-to-fuel conversion. *Chemical Society Reviews* **2016,** *45* (14), 3781-3810.
11. Amirav, L.; Alivisatos, A. P., Photocatalytic Hydrogen Production with Tunable Nanorod Heterostructures. *The Journal of Physical Chemistry Letters* **2010,** *1* (7), 1051-1054.
12. Kumar, S.; Jones, M.; Lo, S. S.; Scholes, G. D., Nanorod heterostructures showing photoinduced charge separation. *Small* **2007,** *3* (9), 1633-1639.
13. Zaiats, G.; Ikeda, S.; Kinge, S.; Kamat, P. V., Quantum Dot Light-Emitting Devices: Beyond Alignment of Energy Levels. *ACS Applied Materials & Interfaces* **2017,** *9* (36), 30741-30745.
14. Carbone, L.; Nobile, C.; De Giorgi, M.; Sala, F. D.; Morello, G.; Pompa, P.; Hytch, M.; Snoeck, E.; Fiore, A.; Franchini, I. R.; Nadasan, M.; Silvestre, A. F.; Chiodo, L.; Kudera, S.; Cingolani, R.; Krahne, R.; Manna, L., Synthesis and Micrometer-Scale Assembly of Colloidal CdSe/CdS Nanorods Prepared by a Seeded Growth Approach. *Nano Letters* **2007,** *7* (10), 2942-2950.
15. Sitt, A.; Sala, F. D.; Menagen, G.; Banin, U., Multiexciton Engineering in Seeded Core/Shell Nanorods: Transfer from Type-I to Quasi-type-II Regimes. *Nano Letters* **2009,** *9* (10), 3470-3476.
16. Luo, Y.; Wang, L.-W., Electronic Structures of the CdSe/CdS Core−Shell Nanorods. *ACS Nano* **2010,** *4* (1), 91-98.
17. Wu, K.; Rodríguez-Córdoba, W.; Lian, T., Exciton Localization and Dissociation Dynamics in CdS and CdS–Pt Quantum Confined Nanorods: Effect of Nonuniform Rod Diameters. *The Journal of Physical Chemistry B* **2014,** *118* (49), 14062-14069.
18. Wu, K.; Hill, L. J.; Chen, J.; McBride, J. R.; Pavlopolous, N. G.; Richey, N. E.; Pyun, J.; Lian, T., Universal Length Dependence of Rod-to-Seed Exciton Localization Efficiency in Type I and Quasi-Type II CdSe@CdS Nanorods. *ACS Nano* **2015,** *9* (4), 4591-4599.
19. Wu, K.; Li, Q.; Du, Y.; Chen, Z.; Lian, T., Ultrafast exciton quenching by energy and electron transfer in colloidal CdSe nanosheet-Pt heterostructures. *Chemical Science* **2015,** *6* (2), 1049-1054.

20. Wu, K.; Li, Q.; Jia, Y.; McBride, J. R.; Xie, Z.-x.; Lian, T., Efficient and Ultrafast Formation of Long-Lived Charge-Transfer Exciton State in Atomically Thin Cadmium Selenide/Cadmium Telluride Type-II Heteronanosheets. *ACS Nano* **2015,** *9* (1), 961-968.
21. Wu, K.; Rodríguez-Córdoba, W. E.; Liu, Z.; Zhu, H.; Lian, T., Beyond Band Alignment: Hole Localization Driven Formation of Three Spatially Separated Long-Lived Exciton States in CdSe/CdS Nanorods. *ACS Nano* **2013,** *7* (8), 7173-7185.
22. Yoskovitz, E.; Menagen, G.; Sitt, A.; Lachman, E.; Banin, U., Nanoscale Near-Field Imaging of Excitons in Single Heterostructured Nanorods. *Nano Letters* **2010,** *10* (8), 3068-3072.
23. Liu, Z.; Ricks, A. M.; Wang, H.; Song, N.; Fan, F.; Zou, S.; Lian, T., High-Resolution Imaging of Electric Field Enhancement and Energy-Transfer Quenching by a Single Silver Nanowire Using QD-Modified AFM Tips. *The Journal of Physical Chemistry Letters* **2013,** *4* (14), 2284-2291.
24. Liu, Z.; Zhu, H.; Song, N.; Lian, T., Probing Spatially Dependent Photoinduced Charge Transfer Dynamics to TiO2 Nanoparticles Using Single Quantum Dot Modified Atomic Force Microscopy Tips. *Nano Letters* **2013,** *13* (11), 5563-5569.
25. Ash, E. A.; Nicholls, G., Super-resolution Aperture Scanning Microscope. *Nature* **1972,** *237* (5357), 510-512.
26. Begley, R. F.; Harvey, A. B.; Byer, R. L., Coherent anti‐Stokes Raman spectroscopy. *Applied Physics Letters* **1974,** *25* (7), 387-390.
27. Taubner, T.; Hillenbrand, R.; Keilmann, F., Nanoscale polymer recognition by spectral signature in scattering infrared near-field microscopy. *Applied Physics Letters* **2004,** *85* (21), 5064-5066.
28. Huang, B.; Bates, M.; Zhuang, X., Super-resolution fluorescence microscopy. *Annual review of biochemistry* **2009,** *78*, 993-1016.
29. Huang, B.; Babcock, H.; Zhuang, X., Breaking the Diffraction Barrier: Super-Resolution Imaging of Cells. *Cell* **2010,** *143* (7), 1047-1058.
30. Bates, M.; Jones, S. A.; Zhuang, X., Stochastic optical reconstruction microscopy (STORM): a method for superresolution fluorescence imaging. *Cold Spring Harbor Protocols* **2013,** *2013* (6), pdb. top075143.
31. Xie, X. S., Single-molecule spectroscopy and dynamics at room temperature. *Accounts of chemical research* **1996,** *29* (12), 598-606.
32. Yoskovitz, E.; Hadar, I.; Sitt, A.; Lieberman, I.; Banin, U., Interplay of Quenching and Enhancement Effects in Apertureless Near-Field Fluorescence Imaging of Single Nanoparticles. *The Journal of Physical Chemistry C* **2011,** *115* (32), 15834-15844.
33. Xie, C.; Mu, C.; Cox, J. R.; Gerton, J. M., Tip-enhanced fluorescence microscopy of high-density samples. *Applied Physics Letters* **2006,** *89* (14), 143117.
34. Stöckle, R. M.; Suh, Y. D.; Deckert, V.; Zenobi, R., Nanoscale chemical analysis by tip-enhanced Raman spectroscopy. *Chemical Physics Letters* **2000,** *318* (1), 131-136.
35. Pettinger, B.; Ren, B.; Picardi, G.; Schuster, R.; Ertl, G., Nanoscale probing of adsorbed species by tip-enhanced Raman spectroscopy. *Physical review letters* **2004,** *92* (9), 096101.
36. Steidtner, J.; Pettinger, B., Tip-enhanced Raman spectroscopy and microscopy on single dye molecules with 15 nm resolution. *Physical Review Letters* **2008,** *100* (23), 236101.
37. Li, J. F.; Huang, Y. F.; Ding, Y.; Yang, Z. L.; Li, S. B.; Zhou, X. S.; Fan, F. R.; Zhang, W.; Zhou, Z. Y.; Ren, B., Shell-isolated nanoparticle-enhanced Raman spectroscopy. *nature* **2010,** *464* (7287), 392-395.
38. Zhang, Z.; Sheng, S.; Wang, R.; Sun, M., Tip-enhanced Raman spectroscopy. ACS Publications: 2016.

39. Dazzi, A.; Prater, C. B.; Hu, Q.; Chase, D. B.; Rabolt, J. F.; Marcott, C., AFM–IR: Combining Atomic Force Microscopy and Infrared Spectroscopy for Nanoscale Chemical Characterization. *Appl. Spectrosc.* **2012,** *66* (12), 1365-1384.
40. Muller, E. A.; Pollard, B.; Raschke, M. B., Infrared Chemical Nano-Imaging: Accessing Structure, Coupling, and Dynamics on Molecular Length Scales. *The Journal of Physical Chemistry Letters* **2015,** *6* (7), 1275-1284.
41. Wang, L.; Xu, X. G., Scattering-type scanning near-field optical microscopy with reconstruction of vertical interaction. **2015,** *6*, 8973.
42. Fu, W.; Zhang, W., Hybrid AFM for Nanoscale Physicochemical Characterization: Recent Development and Emerging Applications. *Small* **2017,** *13* (11), n/a-n/a.
43. Gross, L.; Mohn, F.; Moll, N.; Liljeroth, P.; Meyer, G., The Chemical Structure of a Molecule Resolved by Atomic Force Microscopy. *Science* **2009,** *325* (5944), 1110.
44. Zhu, H.; Chen, Z.; Wu, K.; Lian, T., Wavelength dependent efficient photoreduction of redox mediators using type II ZnSe/CdS nanorod heterostructures. *Chemical Science* **2014,** *5* (10), 3905-3914.
45. Wu, K.; Song, N.; Liu, Z.; Zhu, H.; Rodríguez-Córdoba, W.; Lian, T., Interfacial Charge Separation and Recombination in InP and Quasi-Type II InP/CdS Core/Shell Quantum Dot-Molecular Acceptor Complexes. *The Journal of Physical Chemistry A* **2013,** *117* (32), 7561-7570.
46. Yu, W. W.; Qu, L.; Guo, W.; Peng, X., Experimental Determination of the Extinction Coefficient of CdTe, CdSe, and CdS Nanocrystals. *Chemistry of Materials* **2003,** *15* (14), 2854-2860.
47. García-Santamaría, F.; Chen, Y.; Vela, J.; Schaller, R. D.; Hollingsworth, J. A.; Klimov, V. I., Suppressed Auger Recombination in "Giant" Nanocrystals Boosts Optical Gain Performance. *Nano Letters* **2009,** *9* (10), 3482-3488.
48. Zhu, H.; Lian, T., Wavefunction engineering in quantum confined semiconductor nanoheterostructures for efficient charge separation and solar energy conversion. *Energy & Environmental Science* **2012,** *5* (11), 9406-9418.
49. Balet, L. P.; Ivanov, S. A.; Piryatinski, A.; Achermann, M.; Klimov, V. I., Inverted Core/Shell Nanocrystals Continuously Tunable between Type-I and Type-II Localization Regimes. *Nano Letters* **2004,** *4* (8), 1485-1488.
50. Eaton, P.; West, P., *Atomic force microscopy*. Oxford University Press: 2010.
51. Lakowicz, J. R.; Masters, B. R., Principles of fluorescence spectroscopy. *Journal of Biomedical Optics* **2008,** *13* (2), 029901.
52. Li, Q.; Wu, K.; Chen, J.; Chen, Z.; McBride, J. R.; Lian, T., Size-Independent Exciton Localization Efficiency in Colloidal CdSe/CdS Core/Crown Nanosheet Type-I Heterostructures. *ACS Nano* **2016,** *10* (3), 3843-3851.
53. Li, Q.; Zhou, B.; McBride, J. R.; Lian, T., Efficient Diffusive Transport of Hot and Cold Excitons in Colloidal Type II CdSe/CdTe Core/Crown Nanoplatelet Heterostructures. *ACS Energy Letters* **2017,** *2* (1), 174-181.
54. Efros, A. L.; Nesbitt, D. J., Origin and control of blinking in quantum dots. *Nat Nano* **2016,** *11* (8), 661-671.
55. Warman, J. M.; De Haas, M. P.; Van Hovell tot Westerflier, S. W. F. M.; Binsma, J. J. M.; Kolar, Z. I., Electronic processes in semiconductor materials studied by nanosecond time-resolved microwave conductivity. 1. Cadmium sulfide macroscopic crystal. *The Journal of Physical Chemistry* **1989,** *93* (15), 5895-5899.
56. Shinada, M.; Sugano, S., Interband optical transitions in extremely anisotropic semiconductors. I. Bound and unbound exciton absorption. *Journal of the Physical Society of Japan* **1966,** *21* (10), 1936-1946.

57. Schmitt-Rink, S.; Chemla, D.; Miller, D., Theory of transient excitonic optical nonlinearities in semiconductor quantum-well structures. *Physical Review B* **1985,** *32* (10), 6601.
58. Fox, M., *Quantum optics: an introduction*. OUP Oxford: 2006; Vol. 15.
59. Hugall, J. T.; Singh, A.; van Hulst, N. F., Plasmonic Cavity Coupling. *ACS Photonics* **2018,** *5* (1), 43-53.
60. Ebbesen, T. W., Hybrid Light–Matter States in a Molecular and Material Science Perspective. *Accounts of Chemical Research* **2016,** *49* (11), 2403-2412.
61. Houdré, R., Early stages of continuous wave experiments on cavity-polaritons. *physica status solidi (b)* **2005,** *242* (11), 2167-2196.
62. Thomas, A.; Jayachandran, A.; Lethuillier-Karl, L.; Vergauwe, R. M.; Nagarajan, K.; Devaux, E.; Genet, C.; Moran, J.; Ebbesen, T. W., Ground state chemistry under vibrational strong coupling: dependence of thermodynamic parameters on the Rabi splitting energy. *Nanophotonics* **2020,** *9* (2), 249-255.
63. Bahsoun, H.; Chervy, T.; Thomas, A.; Börjesson, K.; Hertzog, M.; George, J.; Devaux, E.; Genet, C.; Hutchison, J. A.; Ebbesen, T. W., Electronic Light–Matter Strong Coupling in Nanofluidic Fabry–Pérot Cavities. *ACS Photonics* **2017**.
64. Zhong, X.; Chervy, T.; Wang, S.; George, J.; Thomas, A.; Hutchison, J. A.; Devaux, E.; Genet, C.; Ebbesen, T. W., Non-Radiative Energy Transfer Mediated by Hybrid Light-Matter States. *Angewandte Chemie* **2016,** *128* (21), 6310-6314.
65. Thomas, A.; George, J.; Shalabney, A.; Dryzhakov, M.; Varma, S. J.; Moran, J.; Chervy, T.; Zhong, X.; Devaux, E.; Genet, C.; Hutchison, J. A.; Ebbesen, T. W., Ground-State Chemical Reactivity under Vibrational Coupling to the Vacuum Electromagnetic Field. *Angewandte Chemie* **2016,** *128* (38), 11634-11638.
66. George, J.; Wang, S.; Chervy, T.; Canaguier-Durand, A.; Schaeffer, G.; Lehn, J.-M.; Hutchison, J. A.; Genet, C.; Ebbesen, T. W., Ultra-strong coupling of molecular materials: spectroscopy and dynamics. *Faraday Discussions* **2015,** *178* (0), 281-294.
67. Salomon, A.; Wang, S.; Hutchison James, A.; Genet, C.; Ebbesen Thomas, W., Strong Light-Molecule Coupling on Plasmonic Arrays of Different Symmetry. *ChemPhysChem* **2013,** *14* (9), 1882-1886.
68. Hutchison, J. A.; Schwartz, T.; Genet, C.; Devaux, E.; Ebbesen, T. W., Modifying Chemical Landscapes by Coupling to Vacuum Fields. *Angewandte Chemie International Edition* **2012,** *51* (7), 1592-1596.
69. Orgiu, E.; George, J.; Hutchison, J. A.; Devaux, E.; Dayen, J. F.; Doudin, B.; Stellacci, F.; Genet, C.; Schachenmayer, J.; Genes, C.; Pupillo, G.; Samorì, P.; Ebbesen, T. W., Conductivity in organic semiconductors hybridized with the vacuum field. *Nature Materials* **2015,** *14* (11), 1123-1129.
70. Shcherbakov, M. R.; Werner, K.; Fan, Z.; Talisa, N.; Chowdhury, E.; Shvets, G., Photon acceleration and tunable broadband harmonics generation in nonlinear time-dependent metasurfaces. *Nature Communications* **2019,** *10* (1), 1345.
71. Lather, J.; Bhatt, P.; Thomas, A.; Ebbesen, T. W.; George, J., Cavity catalysis by cooperative vibrational strong coupling of reactant and solvent molecules. *Angewandte Chemie International Edition* **2019,** *58* (31), 10635-10638.
72. Xiang, B.; Ribeiro, R. F.; Dunkelberger, A. D.; Wang, J.; Li, Y.; Simpkins, B. S.; Owrutsky, J. C.; Yuen-Zhou, J.; Xiong, W., Two-dimensional infrared spectroscopy of vibrational polaritons. *Proceedings of the National Academy of Sciences* **2018**.
73. Ribeiro, R. F.; Martínez-Martínez, L. A.; Du, M.; Campos-Gonzalez-Angulo, J.; Yuen-Zhou, J., Polariton Chemistry: controlling molecular dynamics with optical cavities. *arXiv preprint arXiv:1802.08681* **2018**.

74. Eizner, E.; Brodeur, J.; Barachati, F.; Sridharan, A.; Kéna-Cohen, S., Organic Photodiodes with an Extended Responsivity Using Ultrastrong Light–Matter Coupling. *ACS Photonics* **2018**.
75. Dunkelberger, A. D.; Davidson Ii, R. B.; Ahn, W.; Simpkins, B. S.; Owrutsky, J. C., Ultrafast Transmission Modulation and Recovery via Vibrational Strong Coupling. *The Journal of Physical Chemistry A* **2018,** *122* (4), 965-971.
76. Dovzhenko, D. S.; Ryabchuk, S. V.; Rakovich, Y. P.; Nabiev, I. R., Light-matter interaction in the strong coupling regime: configurations, conditions, and applications. *Nanoscale* **2018**.
77. Zhong, X.; Chervy, T.; Zhang, L.; Thomas, A.; George, J.; Genet, C.; Hutchison James, A.; Ebbesen Thomas, W., Energy Transfer between Spatially Separated Entangled Molecules. *Angewandte Chemie International Edition* **2017,** *56* (31), 9034-9038.
78. Saurabh, P.; Mukamel, S., Two-dimensional infrared spectroscopy of vibrational polaritons of molecules in an optical cavity. *The Journal of Chemical Physics* **2016,** *144* (12), 124115.
79. Herrera, F.; Spano, F. C., Cavity-Controlled Chemistry in Molecular Ensembles. *Physical Review Letters* **2016,** *116* (23), 238301.
80. George, J.; Chervy, T.; Shalabney, A.; Devaux, E.; Hiura, H.; Genet, C.; Ebbesen, T. W., Multiple Rabi Splittings under Ultrastrong Vibrational Coupling. *Physical Review Letters* **2016,** *117* (15), 153601.
81. Flatten, L. C.; Christodoulou, S.; Patel, R. K.; Buccheri, A.; Coles, D. M.; Reid, B. P. L.; Taylor, R. A.; Moreels, I.; Smith, J. M., Strong Exciton–Photon Coupling with Colloidal Nanoplatelets in an Open Microcavity. *Nano Letters* **2016,** *16* (11), 7137-7141.
82. Wang, S.; Chervy, T.; George, J.; Hutchison, J. A.; Genet, C.; Ebbesen, T. W., Quantum Yield of Polariton Emission from Hybrid Light-Matter States. *The Journal of Physical Chemistry Letters* **2014,** *5* (8), 1433-1439.
83. Long, J. P.; Simpkins, B., Coherent coupling between a molecular vibration and Fabry–Perot optical cavity to give hybridized states in the strong coupling limit. *Acs Photonics* **2014,** *2* (1), 130-136.
84. Coles, D. M.; Somaschi, N.; Michetti, P.; Clark, C.; Lagoudakis, P. G.; Savvidis, P. G.; Lidzey, D. G., Polariton-mediated energy transfer between organic dyes in a strongly coupled optical microcavity. *Nature Materials* **2014,** *13*, 712.
85. Coles, D. M.; Grant, R. T.; Lidzey, D. G.; Clark, C.; Lagoudakis, P. G., Imaging the polariton relaxation bottleneck in strongly coupled organic semiconductor microcavities. *Physical Review B* **2013,** *88* (12), 121303.
86. Westmoreland, D. E.; McClelland, K. P.; Perez, K. A.; Schwabacher, J. C.; Zhang, Z.; Weiss, E. A., Properties of quantum dots coupled to plasmons and optical cavities. *The Journal of Chemical Physics* **2019,** *151* (21), 210901.
87. Wang, X.; Shoaib, M.; Wang, X.; Zhang, X.; He, M.; Luo, Z.; Zheng, W.; Li, H.; Yang, T.; Zhu, X.; Ma, L.; Pan, A., High-Quality In-Plane Aligned CsPbX3 Perovskite Nanowire Lasers with Composition-Dependent Strong Exciton–Photon Coupling. *ACS Nano* **2018**.
88. Kim, J.; Carnemolla, E. G.; DeVault, C.; Shaltout, A. M.; Faccio, D.; Shalaev, V. M.; Kildishev, A. V.; Ferrera, M.; Boltasseva, A., Dynamic Control of Nanocavities with Tunable Metal Oxides. *Nano Letters* **2018,** *18* (2), 740-746.
89. Dunkelberger, A. D.; Ellis, C. T.; Ratchford, D. C.; Giles, A. J.; Kim, M.; Kim, C. S.; Spann, B. T.; Vurgaftman, I.; Tischler, J. G.; Long, J. P.; Glembocki, O. J.; Owrutsky, J. C.; Caldwell, J. D., Active tuning of surface phonon polariton resonances via carrier photoinjection. *Nature Photonics* **2018,** *12* (1), 50-56.

90. Du, W.; Zhang, S.; Shi, J.; Chen, J.; Wu, Z.; Mi, Y.; Liu, Z.; Li, Y.; Sui, X.; Wang, R.; Qiu, X.; Wu, T.; Xiao, Y.; Zhang, Q.; Liu, X., Strong Exciton–Photon Coupling and Lasing Behavior in All-Inorganic CsPbBr3 Micro/Nanowire Fabry-Pérot Cavity. *ACS Photonics* **2018,** *5* (5), 2051-2059.
91. Chen, X.; Chen, Y.-H.; Qin, J.; Zhao, D.; Ding, B.; Blaikie, R. J.; Qiu, M., Mode Modification of Plasmonic Gap Resonances Induced by Strong Coupling with Molecular Excitons. *Nano Letters* **2017,** *17* (5), 3246-3251.
92. Wang, S.; Li, S.; Chervy, T.; Shalabney, A.; Azzini, S.; Orgiu, E.; Hutchison, J. A.; Genet, C.; Samorì, P.; Ebbesen, T. W., Coherent Coupling of WS2 Monolayers with Metallic Photonic Nanostructures at Room Temperature. *Nano Letters* **2016,** *16* (7), 4368-4374.
93. Zhang, C.; Lu, Y.; Ni, Y.; Li, M.; Mao, L.; Liu, C.; Zhang, D.; Ming, H.; Wang, P., Plasmonic Lasing of Nanocavity Embedding in Metallic Nanoantenna Array. *Nano Letters* **2015,** *15* (2), 1382-1387.
94. Schlather, A. E.; Large, N.; Urban, A. S.; Nordlander, P.; Halas, N. J., Near-Field Mediated Plexcitonic Coupling and Giant Rabi Splitting in Individual Metallic Dimers. *Nano Letters* **2013,** *13* (7), 3281-3286.
95. Barth, M.; Schietinger, S.; Fischer, S.; Becker, J.; Nüsse, N.; Aichele, T.; Löchel, B.; Sönnichsen, C.; Benson, O., Nanoassembled Plasmonic-Photonic Hybrid Cavity for Tailored Light-Matter Coupling. *Nano Letters* **2010,** *10* (3), 891-895.
96. Tsintzos, S. I.; Pelekanos, N. T.; Konstantinidis, G.; Hatzopoulos, Z.; Savvidis, P. G., A GaAs polariton light-emitting diode operating near room temperature. *Nature* **2008,** *453*, 372.
97. Okada, D.; Azzini, S.; Nishioka, H.; Ichimura, A.; Tsuji, H.; Nakamura, E.; Sasaki, F.; Genet, C.; Ebbesen, T. W.; Yamamoto, Y., π-Electronic Co-crystal Microcavities with Selective Vibronic-Mode Light Amplification: Toward Förster Resonance Energy Transfer Lasing. *Nano letters* **2018,** *18* (7), 4396-4402.
98. Chervy, T.; Thomas, A.; Akiki, E.; Vergauwe, R. M.; Shalabney, A.; George, J.; Devaux, E.; Hutchison, J. A.; Genet, C.; Ebbesen, T. W., Vibro-polaritonic IR emission in the strong coupling regime. *ACS Photonics* **2018,** *5* (1), 217-224.
99. Hertzog, M.; Rudquist, P.; Hutchison James, A.; George, J.; Ebbesen Thomas, W.; Börjesson, K., Voltage-Controlled Switching of Strong Light–Matter Interactions using Liquid Crystals. *Chemistry – A European Journal* **2017,** *23* (72), 18166-18170.
100. Chervy, T.; Thomas, A.; Akiki, E.; Vergauwe, R. M. A.; Shalabney, A.; George, J.; Devaux, E.; Hutchison, J. A.; Genet, C.; Ebbesen, T. W., Vibro-Polaritonic IR Emission in the Strong Coupling Regime. *ACS Photonics* **2017**.
101. Vergauwe, R. M. A.; George, J.; Chervy, T.; Hutchison, J. A.; Shalabney, A.; Torbeev, V. Y.; Ebbesen, T. W., Quantum Strong Coupling with Protein Vibrational Modes. *The Journal of Physical Chemistry Letters* **2016,** *7* (20), 4159-4164.
102. Chervy, T.; Xu, J.; Duan, Y.; Wang, C.; Mager, L.; Frerejean, M.; Münninghoff, J. A. W.; Tinnemans, P.; Hutchison, J. A.; Genet, C.; Rowan, A. E.; Rasing, T.; Ebbesen, T. W., High-Efficiency Second-Harmonic Generation from Hybrid Light-Matter States. *Nano Letters* **2016,** *16* (12), 7352-7356.
103. Shalabney, A.; George, J.; Hutchison, J.; Pupillo, G.; Genet, C.; Ebbesen, T. W., Coherent coupling of molecular resonators with a microcavity mode. *Nature Communications* **2015,** *6*, 5981.
104. Shalabney, A.; George, J.; Hiura, H.; Hutchison, J. A.; Genet, C.; Hellwig, P.; Ebbesen, T. W., Enhanced Raman Scattering from Vibro-Polariton Hybrid States. *Angewandte Chemie International Edition* **2015,** *54* (27), 7971-7975.
105. Orgiu, E.; George, J.; Hutchison, J. A.; Devaux, E.; Dayen, J. F.; Doudin, B.; Stellacci, F.; Genet, C.; Schachenmayer, J.; Genes, C.; Pupillo, G.; Samorì, P.; Ebbesen, T. W., Conductivity in organic semiconductors hybridized with the vacuum field. *Nature Materials* **2015,** *14*, 1123.

106. George, J.; Shalabney, A.; Hutchison, J. A.; Genet, C.; Ebbesen, T. W., Liquid-Phase Vibrational Strong Coupling. *The Journal of Physical Chemistry Letters* **2015,** *6* (6), 1027-1031.
107. Wang, S.; Mika, A.; Hutchison, J. A.; Genet, C.; Jouaiti, A.; Hosseini, M. W.; Ebbesen, T. W., Phase transition of a perovskite strongly coupled to the vacuum field. *Nanoscale* **2014,** *6* (13), 7243-7248.
108. Schwartz, T.; Hutchison, J. A.; Léonard, J.; Genet, C.; Haacke, S.; Ebbesen, T. W., Polariton Dynamics under Strong Light–Molecule Coupling. *ChemPhysChem* **2013,** *14* (1), 125-131.
109. Hutchison James, A.; Liscio, A.; Schwartz, T.; Canaguier‐Durand, A.; Genet, C.; Palermo, V.; Samorì, P.; Ebbesen Thomas, W., Tuning the Work‐Function Via Strong Coupling. *Advanced Materials* **2013,** *25* (17), 2481-2485.
110. Schwartz, T.; Hutchison, J. A.; Genet, C.; Ebbesen, T. W., Reversible Switching of Ultrastrong Light-Molecule Coupling. *Physical Review Letters* **2011,** *106* (19), 196405.
111. Salomon, A.; Genet, C.; Ebbesen Thomas , W., Molecule–Light Complex: Dynamics of Hybrid Molecule–Surface Plasmon States. *Angewandte Chemie International Edition* **2009,** *48* (46), 8748-8751.
112. Dintinger, J.; Klein, S.; Bustos, F.; Barnes, W. L.; Ebbesen, T. W., Strong coupling between surface plasmon-polaritons and organic molecules in subwavelength hole arrays. *Physical Review B* **2005,** *71* (3), 035424.
113. Barnes, W. L.; Dereux, A.; Ebbesen, T. W., Surface plasmon subwavelength optics. *Nature* **2003,** *424*, 824.
114. Martín-Moreno, L.; García-Vidal, F. J.; Lezec, H. J.; Pellerin, K. M.; Thio, T.; Pendry, J. B.; Ebbesen, T. W., Theory of Extraordinary Optical Transmission through Subwavelength Hole Arrays. *Physical Review Letters* **2001,** *86* (6), 1114-1117.
115. Ebbesen, T. W.; Lezec, H. J.; Ghaemi, H. F.; Thio, T.; Wolff, P. A., Extraordinary optical transmission through sub-wavelength hole arrays. *Nature* **1998,** *391*, 667.
116. Dunkelberger, A. D.; Spann, B. T.; Fears, K. P.; Simpkins, B. S.; Owrutsky, J. C., Modified relaxation dynamics and coherent energy exchange in coupled vibration-cavity polaritons. *Nature Communications* **2016,** *7*, 13504.
117. Zhang, R.; Peng, X.; Jiao, Z.; Luo, T.; Zhou, C.; Yang, X.; Ren, Z., Flexible high-resolution broadband sum-frequency generation vibrational spectroscopy for intrinsic spectral line widths. *The Journal of Chemical Physics* **2019,** *150* (7), 074702.
118. Lagutchev, A.; Hambir, S. A.; Dlott, D. D., Nonresonant Background Suppression in Broadband Vibrational Sum-Frequency Generation Spectroscopy. *The Journal of Physical Chemistry C* **2007,** *111* (37), 13645-13647.
119. Ismail, N.; Kores, C. C.; Geskus, D.; Pollnau, M., Fabry-Pérot resonator: spectral line shapes, generic and related Airy distributions, linewidths, finesses, and performance at low or frequency-dependent reflectivity. *Opt. Express* **2016,** *24* (15), 16366-16389.
120. Terdale, S.; Tantray, A., Spectroscopic study of the dimerization of rhodamine 6G in water and different organic solvents. *Journal of Molecular Liquids* **2017,** *225*, 662-671.
121. Ribeiro, R. F.; Dunkelberger, A. D.; Xiang, B.; Xiong, W.; Simpkins, B. S.; Owrutsky, J. C.; Yuen-Zhou, J., Theory for nonlinear spectroscopy of vibrational polaritons. *arXiv preprint arXiv:1711.11242* **2017**.
122. Simpkins, B. S.; Fears, K. P.; Dressick, W. J.; Spann, B. T.; Dunkelberger, A. D.; Owrutsky, J. C., Spanning Strong to Weak Normal Mode Coupling between Vibrational and Fabry–Pérot Cavity Modes through Tuning of Vibrational Absorption Strength. *ACS Photonics* **2015,** *2* (10), 1460-1467.
123. Khitrova, G.; Gibbs, H. M.; Jahnke, F.; Kira, M.; Koch, S. W., Nonlinear optics of normal-mode-coupling semiconductor microcavities. *Reviews of Modern Physics* **1999,** *71* (5), 1591-1639.

124. Zhu, Y.; Gauthier, D. J.; Morin, S. E.; Wu, Q.; Carmichael, H. J.; Mossberg, T. W., Vacuum Rabi splitting as a feature of linear-dispersion theory: Analysis and experimental observations. *Physical Review Letters* **1990,** *64* (21), 2499-2502.
125. Lu, Q.; Jiao, F., Electrochemical CO2 reduction: Electrocatalyst, reaction mechanism, and process engineering. *Nano Energy* **2016,** *29*, 439-456.
126. Aresta, M.; Dibenedetto, A.; Angelini, A., Catalysis for the valorization of exhaust carbon: from CO2 to chemicals, materials, and fuels. Technological use of CO2. *Chem. Rev.* **2013,** *114*, 1709-1742.
127. Pan, Y.; Lin, R.; Chen, Y.; Liu, S.; Zhu, W.; Cao, X.; Chen, W.; Wu, K.; Cheong, W.-C.; Wang, Y.; Zheng, L.; Luo, J.; Lin, Y.; Liu, Y.; Liu, C.; Li, J.; Lu, Q.; Chen, X.; Wang, D.; Peng, Q.; Chen, C.; Li, Y., Design of Single-Atom Co–N5 Catalytic Site: A Robust Electrocatalyst for CO2 Reduction with Nearly 100% CO Selectivity and Remarkable Stability. *J. Am. Chem. Soc.* **2018,** *140*, 4218-4221.
128. Lum, Y.; Ager, J. W., Stability of Residual Oxides in Oxide-Derived Copper Catalysts for Electrochemical CO2 Reduction Investigated with 18O Labeling. *Angew. Chem.* **2018,** *57*, 551-554.
129. Trindell, J. A.; Clausmeyer, J.; Crooks, R. M., Size Stability and H2/CO Selectivity for Au Nanoparticles during Electrocatalytic CO2 Reduction. *J. Am. Chem. Soc.* **2017,** *139*, 16161-16167.
130. Weng, Z.; Jiang, J.; Wu, Y.; Wu, Z.; Guo, X.; Materna, K. L.; Liu, W.; Batista, V. S.; Brudvig, G. W.; Wang, H., Electrochemical CO2 Reduction to Hydrocarbons on a Heterogeneous Molecular Cu Catalyst in Aqueous Solution. *J. Am. Chem. Soc.* **2016,** *138*, 8076-8079.
131. Matsubu, J. C.; Yang, V. N.; Christopher, P., Isolated Metal Active Site Concentration and Stability Control Catalytic CO2 Reduction Selectivity. *J. Am. Chem. Soc.* **2015,** *137*, 3076-3084.
132. Chen, C. S.; Handoko, A. D.; Wan, J. H.; Ma, L.; Ren, D.; Yeo, B. S., Stable and selective electrochemical reduction of carbon dioxide to ethylene on copper mesocrystals. *Catal. Sci. Technol.* **2015,** *5*, 161-168.
133. Kang, P.; Cheng, C.; Chen, Z.; Schauer, C. K.; Meyer, T. J.; Brookhart, M., Selective Electrocatalytic Reduction of CO2 to Formate by Water-Stable Iridium Dihydride Pincer Complexes. *J. Am. Chem. Soc.* **2012,** *134*, 5500-5503.
134. Won, D. H.; Shin, H.; Koh, J.; Chung, J.; Lee, H. S.; Kim, H.; Woo, S. I., Highly Efficient, Selective, and Stable CO2 Electroreduction on a Hexagonal Zn Catalyst. *Angew. Chem.* **2016,** *55*, 9297-9300.
135. Wu, J.; Yadav, R. M.; Liu, M.; Sharma, P. P.; Tiwary, C. S.; Ma, L.; Zou, X.; Zhou, X.-D.; Yakobson, B. I.; Lou, J.; Ajayan, P. M., Achieving Highly Efficient, Selective, and Stable CO2 Reduction on Nitrogen-Doped Carbon Nanotubes. *ACS Nano* **2015,** *9*, 5364-5371.
136. Li, C. W.; Kanan, M. W., CO2 Reduction at Low Overpotential on Cu Electrodes Resulting from the Reduction of Thick Cu2O Films. *J. Am. Chem. Soc.* **2012,** *134*, 7231-7234.
137. Hawecker, J.; Lehn, J.-M.; Ziessel, R., Electrocatalytic reduction of carbon dioxide mediated by Re (bipy)(CO) 3 Cl (bipy= 2, 2′-bipyridine). *J. Chem. Soc., Chem. Commun.* **1984,** (6), 328-330.
138. Sun, C.; Gobetto, R.; Nervi, C., Recent advances in catalytic CO2 reduction by organometal complexes anchored on modified electrodes. *New Journal of Chemistry* **2016,** *40* (7), 5656-5661.
139. Serna, P.; Gates, B. C., Molecular Metal Catalysts on Supports: Organometallic Chemistry Meets Surface Science. *Acc. Chem. Res.* **2014,** *47*, 2612-2620.
140. Aragonès, A. C.; Haworth, N. L.; Darwish, N.; Ciampi, S.; Bloomfield, N. J.; Wallace, G. G.; Diez-Perez, I.; Coote, M. L., Electrostatic catalysis of a Diels–Alder reaction. *Nature* **2016,** *531*, 88.
141. Fried, S. D.; Bagchi, S.; Boxer, S. G., Extreme electric fields power catalysis in the active site of ketosteroid isomerase. *Science* **2014,** *346*, 1510-1514.

142. Peng, Q.; Chen, J.; Ji, H.; Morita, A.; Ye, S., Origin of the Overpotential for the Oxygen Evolution Reaction on a Well-Defined Graphene Electrode Probed by in Situ Sum Frequency Generation Vibrational Spectroscopy. *J. Am. Chem. Soc.* **2018,** *140*, 15568-15571.
143. Clark, M. L.; Ge, A.; Videla, P. E.; Rudshteyn, B.; Miller, C. J.; Song, J.; Batista, V. S.; Lian, T.; Kubiak, C. P., CO2 Reduction Catalysts on Gold Electrode Surfaces Influenced by Large Electric Fields. *J. Am. Chem. Soc.* **2018,** *140*, 17643-17655.
144. Ge, A.; Videla, P. E.; Lee, G. L.; Rudshteyn, B.; Song, J.; Kubiak, C. P.; Batista, V. S.; Lian, T., Interfacial Structure and Electric Field Probed by in Situ Electrochemical Vibrational Stark Effect Spectroscopy and Computational Modeling. *J. Phys. CHem. C* **2017,** *121*, 18674-18682.
145. Shen, Y.-R., The principles of nonlinear optics. *New York, Wiley-Interscience, 1984, 575 p.* **1984**.
146. Zhuang, X.; Miranda, P.; Kim, D.; Shen, Y., Mapping Molecular Orientation and Conformation at Interfaces by Surface Nonlinear Optics. *Phys. Rev. B* **1999,** *59*, 12632.
147. Wang*, H.-F.; Gan, W.; Lu†‡ §, R.; Rao†‡¶, Y.; Wu, B.-H., Quantitative spectral and orientational analysis in surface sum frequency generation vibrational spectroscopy (SFG-VS). *Int. Rev. Phys. Chem.* **2005,** *24*, 191-256.
148. Shen, Y., Phase-Sensitive Sum-Frequency Spectroscopy. *Annu. Rev. Phys. Chem.* **2013,** *64*, 129-150.
149. Ge, A.; Rudshteyn, B.; Psciuk, B. T.; Xiao, D.; Song, J.; Anfuso, C. L.; Ricks, A. M.; Batista, V. S.; Lian, T., Surface-induced anisotropic binding of a rhenium CO2-reduction catalyst on rutile TiO2 (110) surfaces. *J. Phys. Chem. C* **2016,** *120*, 20970-20977.
150. Anfuso, C. L.; Snoeberger, R. C.; Ricks, A. M.; Liu, W.; Xiao, D.; Batista, V. S.; Lian, T., Covalent Attachment of a Rhenium Bipyridyl CO2 Reduction Catalyst to Rutile TiO2. *J. Am. Chem. Soc.* **2011,** *133*, 6922-6925.
151. Smieja, J. M.; Kubiak, C. P., Re (bipy-tBu)(CO) 3Cl− improved catalytic activity for reduction of carbon dioxide: IR-spectroelectrochemical and mechanistic studies. *Inorg. Chem.* **2010,** *49*, 9283-9289.
152. Becka, A. M.; Miller, C. J., Electrochemistry at Omega-Hydroxy Thiol Coated Electrodes .4. Comparison of the Double-Layer at Omega-Hydroxy Thiol and Alkanethiol Monolayer Coated Au Electrodes. *J. Phys. Chem.* **1993,** *97* (23), 6233-6239.
153. Bard, A. J.; Faulkner, L. R.; Leddy, J.; Zoski, C. G., *Electrochemical methods: fundamentals and applications*. wiley New York: 1980; Vol. 2.
154. Janek, R. P.; Fawcett, W. R.; Ulman, A., Impedance spectroscopy of self-assembled monolayers on Au (111): evidence for complex double-layer structure in aqueous NaClO4 at the potential of zero charge. *J. Phys. Chem. B* **1997,** *101*, 8550-8558.
155. Kondo, T.; Sumi, T.; Uosaki, K., A rotating gold ring–gold disk electrode study on electrochemical reductive desorption and oxidative readsorption of a self-assembled monolayer of dodecanethiol. *J. Electroanal. Chem.* **2002,** *538*, 59-63.
156. Jacob, J. D. C.; Lee, T. R.; Baldelli, S., In situ vibrational study of the reductive desorption of alkanethiol monolayers on gold by sum frequency generation spectroscopy. *J. Phys. Chem. C* **2014,** *118*, 29126-29134.
157. Yang, D.-F.; Wilde, C.; Morin, M., Studies of the electrochemical removal and efficient re-formation of a monolayer of hexadecanethiol self-assembled at an Au (111) single crystal in aqueous solutions. *Langmuir* **1997,** *13*, 243-249.
158. Widrig, C. A.; Chung, C.; Porter, M. D., The electrochemical desorption of n-alkanethiol monolayers from polycrystalline Au and Ag electrodes. *J. Electroanal. Chem. Interfacial Electrochem.* **1991,** *310*, 335-359.

159. Wei, Q.; Zhou, D.; Bian, H., Molecular structure and adsorption of dimethyl sulfoxide at the air/aqueous solution interface probed by non-resonant second harmonic generation. *Phys. Chem. Chem. Phys.* **2018,** *20*, 11758-11767.
160. Bian, H.-t.; Guo, Y.; Wang, H.-f., Non-parabolic potential dependence of optical second harmonic generation from the Si (111) electrode/electrolyte interface. *Phys. Chem. Chem. Phys.* **2018,** *20*, 29539-29548.
161. Bian, H.-t.; Feng, R.-r.; Xu, Y.-y.; Guo, Y.; Wang, H.-f., Increased interfacial thickness of the NaF, NaCl and NaBr salt aqueous solutions probed with non-resonant surface second harmonic generation (SHG). *Phys. Chem. Chem. Phys.* **2008,** *10*, 4920-4931.
162. Guyot-Sionnest, P.; Tadjeddine, A.; Liebsch, A., Electronic distribution and nonlinear optical response at the metal-electrolyte interface. *Phys. Rev. Lett.* **1990,** *64*, 1678-1681.
163. Guyot‐Sionnest, P.; Tadjeddine, A., Study of Ag (111) and Au (111) electrodes by optical second‐harmonic generation. *J. Chem. Phys.* **1990,** *92*, 734-738.
164. Ramírez, P.; Andreu, R.; Cuesta, Á.; Calzado, C. J.; Calvente, J. J., Determination of the potential of zero charge of Au (111) modified with thiol monolayers. *Anal. Chem.* **2007,** *79*, 6473-6479.
165. Iwami, Y.; Hobara, D.; Yamamoto, M.; Kakiuchi, T., Determination of the potential of zero charge of Au (1 1 1) electrodes modified with thiol self-assembled monolayers using a potential-controlled sessile drop method. *J. Electroanal. Chem.* **2004,** *564*, 77-83.
166. Sondag-Huethorst, J.; Fokkink, L., Potential-dependent wetting of octadecanethiol-modified polycrystalline gold electrodes. *Langmuir* **1992,** *8*, 2560-2566.